Molecular dynamics and experimental study on the adhesion mechanism of polyvinyl alcohol (PVA) fiber in alkali-activated slag/fly ash

Shizhe Zhang [a,1], Eduardo Duque-Redondo [b,c,1], Albina Kostiuchenko [a], Jorge S. Dolado [a,c,d,*], Guang Ye [a,*]

[a] Microlab, Section Materials and Environment, Department of Materials, Mechanics, Management and Design, Faculty of Civil Engineering and Geosciences, Delft University of Technology, Stevinweg 1, 2628 CN, Delft, the Netherlands
[b] Molecular Spectroscopy Laboratory, Department of Physical Chemistry, University of the Basque Country UPV/EHU, Aptdo. 664, 48080 Bilbao, Spain
[c] Donostia International Physics Center (DIPC), Paseo Manuel de Lardizabal 4, 20018 Donostia-San Sebastián, Spain
[d] Centro de Física de Materiales, CFM-CSIC-UPV/EHU, Paseo Manuel de Lardizabal, 5, 20018 San Sebastián, Spain

A B S T R A C T

This paper aims to study the adhesion mechanism of polyvinyl alcohol (PVA) fiber within alkali-activated slag/fly ash (AASF) matrix using molecular dynamics (MD) simulation in combination with systematic experimental characterization. The adhesion of PVA to C-(N-)A-S-H gel with different Ca/(Si+Al) and Al/Si ratios was modeled using MD simulation, with the related adsorption enthalpy calculated and the adhesion mechanism explored. The experimentally attained chemical bonding energy of PVA fiber in AASF coincides well with the simulation results. In both cases, the adhesion enhances primarily with increasing Ca/(Si+Al) ratio of C-(N-)A-S-H gel. Additionally, MD simulation indicates preferential element distributions of Ca around PVA molecule, which was confirmed experimentally by the detection of the Ca-rich C-(N-)A-S-H gel in the interfacial transition zone (ITZ).

This study provides further insights into the adhesion mechanism of PVA fiber to C-(N-)A-S-H gel formed in AASF, which is particularly valuable for the future development of PVA-based high-performance alkali-activated composites.

1. Introduction

Alkali-activation technology has been considered as a promising approach to transforms different wastes and industrial by-products into cement-free building materials. Alkali-activated materials (AAMs) including those geopolymers are derived by the reaction of an alkali metal source (solid or dissolved) with a solid alumino-silicate powder [1,2]. Compared with conventional cementitious binders, AAMs are environmental-friendly with a considerable reduction of global warming potential and embodied energy [3–5]. Meanwhile, AAMs as binder material for concrete could maintain comparable mechanical properties and even better durability under different exposure conditions [6–9]. Therefore, AAMs serve as a promising alternative binder material for sustainable construction and perfectly meet the Sustainable Development Goals (SDGs) by the United Nations. Among all AAMs, the ones based on blast furnace slag, class F fly ash, and their blends are most intensively studied due to the large quantity of annual production as well as the relatively stable chemical compositions of these two solid precursors [1,2,10,11]. Previous studies on the slag/fly ash-based AAMs system, or namely alkali-activated slag/fly ash (AASF), have focused on microstructure development, nature of reaction products as well as mechanical properties [12–16]. The application of AASF for engineering practices has been also greatly promoted.

However, AAMs as binder materials are found to be also inherently (quasi-)brittle like conventional cementitious binder [17–20] and thereby susceptible to cracking. Both alkali-activated fly ash-based concrete [17,18] and alkali-activated slag concrete [19,20] exhibited a higher brittleness than its OPC concrete counterpart with similar compressive strength. Previous studies reported that the brittleness of AASF-based concrete is at least comparable to that of OPC concrete with similar compressive strength [21,22]. As one of the classic approaches in controlling the brittleness of cementitious materials, fiber reinforcement has been researched in AAMs systems and was found to hold promises in achieving advanced fracture and tensile performances [23–26].

Polymeric micro-fibers were effectively used to obtain a composite with extraordinary tensile performance, among which, polyvinyl alcohol (PVA) fiber with good chemical bonding to hydration product and sound mechanical properties has been widely used [23–26]. Particularly, it is applied for the development of high-performance composites such as strain-hardening cementitious composite (SHCC) [27] and strain-hardening geopolymer composite (SHGC) [23–25].

For the development of PVA fiber reinforced cementitious and/or alkali-activated composites such as SHCC and SHGC, the fiber/matrix interface properties are crucial. Many previous studies thereby focused on the characterization and modification of PVA fiber/matrix interface properties and single-fiber pullout tests have been widely used to determine the interface properties [28–30]. Among the interface properties, the chemical bonding energy (G_d) due to adhesion between the PVA fiber and the reaction products plays an essential role. However, the available studies concerning the adhesion of PVA fiber within AAMs are still rare. Only a few experimental studies on the interface bonding properties of PVA fiber in alkali-activated matrices could be found. For instance, Ohno and Li studied the interface properties [23] of PVA fiber in a fly ash-based geopolymer matrix after strength optimization. They found that, in comparison to those in conventional SHCC materials, the value of G_d is almost 5 times higher while the frictional bond and tendency for slip-hardening behavior is considerably lower. Nematollahi et al. tested the interface properties of PVA fiber/matrix properties in alkali-activated fly ash mixtures. The influence of using both sodium and potassium silicate-based activators and the surface oiling treatment on the interface properties were addressed [24]. Besides, the correlations of G_d with frictional bond and slip-hardening behavior were suggested. Additionally, Nematollahi et al. concluded that strong chemical bonding of PVA fiber within a one-part AASF matrix could effectively enhance the fiber-bridging strength of the composite [26]. Zhang et al. investigated the interface properties of PVA fiber within AASF matrices and reported that G_d is predominantly related to microstructure and reaction product chemistry, which could be effectively modified by changing the silicate modulus of alkaline activator [25]. However, the scope of most of these studies is limited to the mesoscale experimental determination of interface properties and their impact on the composite behavior. In all these works, the main purpose of interface characterization relates to the development of SHGC. The adhesion mechanism of PVA fiber within AAMs, however, has seldom been discussed.

Due to the limitations of current experimental techniques at the necessary length-scale, speculation into the interaction between an organic matter (PVA fiber) and an inorganic matrix (AAMs) is not straightforward. As a result, many researchers used molecular dynamics (MD) simulation to provide a complementary understanding of the experimental findings concerning the adhesion at micro/meso scales, which was achieved by looking into the interface interaction to provide insights on the adhesion-related mechanical properties [31]. Most of the times, the adhesion properties were studied by the implementation of molecular dynamics (MD) to calculate critical values of the interaction energy (including adsorption enthalpies). Besides, the interfacial connection mechanism could be also unraveled by investigation of the interaction between organic matter and inorganic matrix using different force fields. Several studies could be found concerning the adhesion properties between the cementitious matrix and different organic matter, which includes polymer fiber [32], polymer additives [33,34], and epoxy resin [35,36]. However, the studies on adhesion between PVA fiber and alkali-activated matrix are still rare. Since the main reaction product in the cementitious matrix and the alkali-activated matrix is not the same, the knowledge on the influence of reaction product chemistry on the adhesion properties of PVA fiber as well as its interaction mechanism with the AAMs system such as AASF is still largely unknown.

This study aims to provide better understanding on the PVA fiber/AASF matrix adhesion mechanism. Through MD simulation, the influence of reaction product chemistry on the PVA fiber adhesion within AASF matrices is modeled and the preferential element distribution around PVA fiber is determined. Furthermore, the corresponding microscale characteristics of adhesion influenced by reaction product chemistry were also studied experimentally through single-fiber pullout tests. Besides, the influence of PVA fiber on the spatial element distribution of reaction products was experimentally confirmed. This study offers new insights into the adhesion properties and adhesion mechanism of PVA fiber within C-(N-)A-S-H type reaction products within AASF and thereby also contributes to the fundamental design basis for the development and tailoring of PVA-SHGC based on alkali-activated matrices.

2. Materials and methods

2.1. MD simulation details

2.1.1. The starting point for MD simulation

Many studies have reported the chemical composition and phases within the reaction products of sodium silicate-based AASF. When the slag content is dominant ($\geq$50 wt%), the AASF is considered to be a high or intermediate calcium AAMs system with typical main reaction products of C-(N-)A-S-H gel along with minor phases like hydrotalcite and possible coexistence of (N,C)-A-S-H gel [3,12,37–39]. The traces of calcium-free N-A-S-H type gel is rarely reported in AASF. This is because N-A-S-H is only stable at low pH values ($<$12) in a Ca-rich alkali-activated system [40]. The system with high pH favors the formation of C-A-S-H type gel to the detriment of N-A-S-H type gel, with the experimental evidence showing the coexistence of C-A-S-H and N-A-S-H leads to degradation of N-A-S-H and its transformation to C-A-S-H until equilibrium conditions are reached [41]. In fact, it has been confirmed by our previous study that the C-(N-)A-S-H gel is the predominant binding phase in sodium silicate-based AASF [39,42]. Consequently, this study focuses on the adhesion between PVA fiber and the C-(N-)A-S-H gel as the main binding phase in AASF.

For the MD simulation, the chemical composition of C-(N-)A-S-H gel by EDX spot analysis in AASF matrices is selected as the starting point for the construction of the C-(N-)A-S-H models. Notably, these AASF matrices share similar mixture designs for experimental testing in the current study [39]. Based on this, five C-(N-)A-S-H models were considered covering various Ca/(Si+Al) and Al/Si ratios, from 0.5 to 1.3 and from 0.25 to 0.5 respectively. Further discussion concerning the correlation between the chemical composition of the C-(N-)A-S-H models and the AASF matrices will be provided in Section 3.4.1.

2.1.2. Construction of the C-(N-)A-S-H model

The C-(N-)A-S-H models were created following the procedure described by Pellenq [43] and refined by Qomi [44], based on the modification of the structure of tobermorite 14 Å minerals. In the construction of the C-(N-)A-S-H model, the restrictions imposed by Kovačević [45] and Kumar [46] in their procedures were also considered to avoid the presence of monomeric species. The construction procedure is shown schematically in Fig. 1.

In the first step, the structure of the tobermorite 14 Å described by Bonaccorsi et al. [47] is taken as the starting point for building the C-(N-)A-S-H model. The unit cell of this mineral is replicated to obtain a simulation box with dimensions in the x, y, and z directions of 5.2 nm $\times$ 6.2 nm $\times$ 3.3 nm, respectively, and periodic boundary conditions (PBC) were applied to approximate to an infinite system. The chemistry of the tobermorite mineral was modified in a second step to reach the desired composition of the C-(N-)A-S-H gel. To this effect, all water molecules were removed from the interlaminar spaces and some bridging silicate groups were deleted randomly. The remaining bridging silicates are partially substituted by aluminates to adjust the Al/Si ratio to values between 0.25 and 0.5. The negative charge generated by the replacement of Si^{4+} by Al^{3+} is compensated by inserting one Na ion per Al. Additionally, Ca is added to match the Ca/(Si+Al) ratio, increasing it from 0.83 (the typical value of tobermorite 14 Å minerals) up to 1.3,
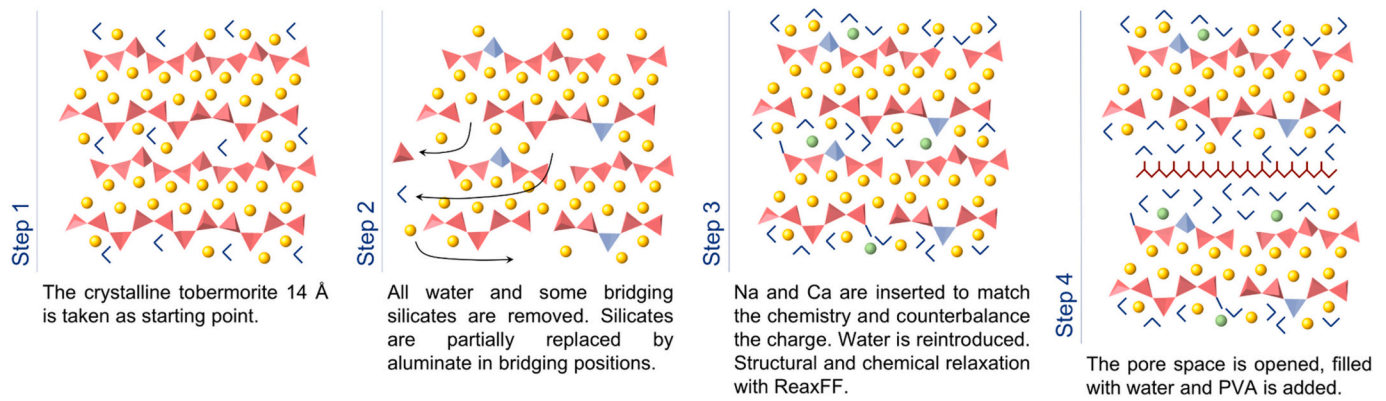
Fig. 1. Schematic procedure of the construction of the C-(N-)A-S-H models.

while no silicate monomers are generated [45,46]. To reach values below 0.83, the interlaminar Ca is replaced by Na ions.

Once the Ca/(Si+Al) and Al/Si ratios are adjusted, water is reintroduced in the pore space using a geometry-based algorithm [48] up to a density of 1 g/cm^3 and the structure was equilibrated in the following step. The LAMMPS code [49] and the force field ReaxFF [50] were used to perform an energy minimization and MD simulations in the isobaric-isothermal ensemble (NPT) at room conditions (300 K and 1 atm) for 5 ns with barostat and thermostat coupling constants of 0.2 and 1 ps, respectively. ReaxFF is a reactive force field that allows the structural and chemical relaxation of the C-(N-)A-S-H gel. Thus, water molecules can dissociate into hydroxyl groups in the new Q^1 sites formed after the bridging silicate deletion [51].

The last step comprises the expansion of the pore space (1.5 nm) to accommodate the PVA molecules. Then, the pore is filled with water and the PVA/C-(N-)A-S-H composite is equilibrated using a combination of CSHFF [52] and CHARMM [53] force fields to describe the C-(N-)A-S-H gel and the PVA fiber. An initial relaxation was conducted in the canonical ensemble (NVT) for 0.5 ns at 300 K with the thermostat coupling constant of 0.1 ps, followed by further equilibration in the isobaric-isothermal ensemble (NPT) at room conditions (300 K and 1 atm) with barostat and thermostat coupling constants of 0.2 and 1 ps, respectively. A final MD simulation, long enough to capture all the properties properly, was carried out in the canonical ensemble for 0.1 μs at 300 K. The lattice parameters and densities of the different PVA/C-(N-)A-S-H composite after equilibration are shown in Table 1.

2.1.3. Construction of the PVA molecules

The Avogadro Builder [54] was employed to create the PVA molecules formed by 100 monomeric units of vinyl alcohol as shown in Fig. 2. The structure of the PVA molecules was equilibrated by performing MD simulations using the LAMMPS simulation package [49]. CHARMM force field [53] was used to describe the bonding and non-bonding interactions in the PVA molecules, while the atomic charges were derived by electrostatic potential (ESP) analysis of DFT results, using the ChelpG scheme [55].

First, energy minimization was performed, relaxing the atomic positions of the molecule and its simulation box. Then, the structure of the PVA molecules was equilibrated in the canonical ensemble (NVT) at 300

K during 2.5 ns, with a time step of 0.5 fs and a thermostat coupling constant of 0.1 ps. Finally, the atomic positions and the volume of the simulation box were further relaxed in the isobaric-isothermal ensemble (NPT) at 300 K and 1 atm for another 2.5 ns with a thermostat and barostat coupling constants of 0.1 ps.

2.1.4. In situ polymerization

The *in situ* polymerization of the C-(N-)A-S-H gel was performed using monomeric species including Ca(OH)$_2$, Si(OH)$_4$, and Al(OH)$_4$Na. The complicated polymerization process from these monomers to C-(N-)A-S-H gel and the interfacial potential reactions between PVA and the monomers are crucial factors to reveal the microstructures of the matrix and the interfacial transition zone (ITZ). GULP was used to perform this *in situ* polymerization, which consists basically placing a PVA fiber and the precursors Ca(OH)$_2$, Si(OH)$_4$, and Al(OH)$_4$Na into a simulation box with dimensions 4 nm × 4 nm × 4 nm in the x, y and z directions, allowing the formation of C-(N-)A-S-H gel under the influence of PVA fiber. To this effect, a combination of the reactive Garofalini potential [56] for the polymerization of the C-(N-)A-S-H gel and CHARMM force field [53] for the PVA molecules was employed. The polymerization requires high temperatures and long simulation times, so the samples were equilibrated in the canonical ensemble (NVT) at 1500 K for 5 ns, with a time step of 0.5 fs and a thermostat coupling constant of 0.5 ps.

2.1.5. Interaction between the PVA fiber and the C-(N-)A-S-H gel

In the MD simulations, the PVA/C-(N-)A-S-H composites are built placing the PVA fiber in the center of the expanded pore at about 0.7 nm from the C-(N-)A-S-H surface. During the relaxation of the system, it is observed that the PVA fiber approaches the C-(N-)A-S-H surface, with the hydroxyl groups pointing towards C-(N-)A-S-H surface. Accordingly, the structural and compositional differences of the C-(N-)A-S-H models with different Ca/Si and Al/Si ratios should influence the interaction with the PVA molecules. Thus, the radial distribution function (RDF) and the coordination number (CN) can provide useful information about the interactions in the PVA/C-(N-)A-S-H composites. The RDF gives the probability of finding an observed particle as a function of a distance, between r and r+dr, from a reference particle, in this way describing the density variation as a function of the distance. It is calculated using the following equation [57]:

Table 1
Lattice parameters and densities for the PVA/C-(N-)A-S-H composites after MD equilibration at the studied Ca/(Si+Al) ratio with Al/Si ratio of 0.5.

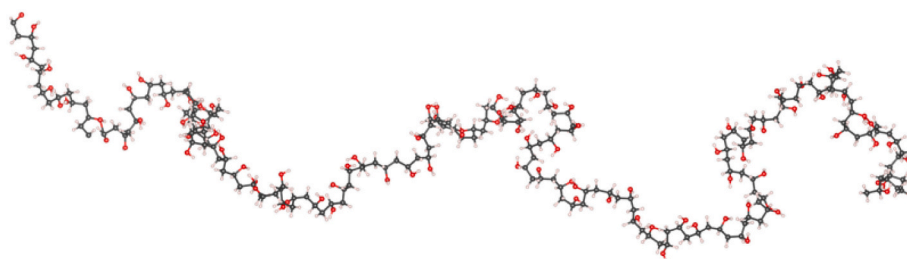| Ca/(Si+Al) ratio	0.5		0.75		1.0		1.1		1.3	
Al/Si ratio	0.25	0.5	0.25	0.5	0.25	0.5	0.25	0.5	0.25	0.5
L_x (nm)	5.181	5.179	5.272	5.215	5.083	5.037	4.972	5.013	4.925	4.877
L_y (nm)	6.062	5.983	6.158	5.973	5.828	5.747	5.790	5.696	5.688	5.544
L_z (nm)	2.975	3.183	2.918	3.061	3.451	3.375	3.061	3.161	2.949	2.911
ρ (g/cm^3)	1.670	1.577	1.697	1.711	1.376	1.526	1.664	1.696	1.758	1.912

Fig. 2. Atomic structure of the PVA molecules.

$$g(r) = \frac{V}{N_i N_j} \sum_i^{N_i} \sum_j^{N_j} \left\langle \delta\left(r - \left| \vec{r_i}(t) - \vec{r_j}(t) \right| \right) \right\rangle_t \qquad (1)$$

where r_i and r_j define the position vectors of the particle i and j. The parameter δ takes the value 1 in the interval $[-w, w]$ (with w being the bin width), otherwise 0. This function can be used to link the microscopic details to macroscopic properties since the computed RDFs can be compared with experimental RDFs obtained from neutron and X-ray diffraction, allowing the validation of the atomic structure of the simulated composites [58]. In this case, the RDFs were computed to study the microscopic adhesion mechanism of the PVA fiber to C-(N-)A-S-H gel and its association with experimental proofs were later discussed in Section 3.4.2.

The integration of the RDF gives the CN, which can be defined as the total number of particles that a reference particle holds as neighbors within a shell between r and r+dr. The CN of a certain atom is given by the following Eq. (2):

$$n(r) = 4\pi \int_r^{r+dr} \rho r^2 g(r) dr \qquad (2)$$

where ρ the atomic density.

In particular, the RDFs and CNs of the hydroxyl groups of the PVA fibers were calculated with the cations and with the oxygen atoms from the C-(N-)A-S-H surfaces to analyze the evolution of the interaction with various Ca/(Si+Al) and Al/Si ratios.

2.2. Experimental testing

2.2.1. Materials and mixture design

The solid precursors were ground granulated blast furnace slag and Class F fly ash according to ASTM 618. Material density for slag is 2890 kg/m³ and 2440 kg/m³ for fly ash. The d50 particle size is 17.88 μm for slag and 33.19 μm for fly ash. The chemical compositions deduced from X-ray Fluorescence along with other properties of precursors (including the loss on ignition (LOI) at 950 °C and the fineness passing 45 μm) are shown in Table 2. As reported in our previous studies [16,25], the main crystalline phases determined by powder X-ray diffraction (XRD) in fly ash are quartz, mullite, and hematite, while the blast furnace slag contains mainly amorphous phases (>95%). The reactivity of fly ash is reflected by its reactive silica content (43.04%) and reactive alumina content (14.51%) as determined by selective chemical dissolution [16]. A polyvinyl alcohol (PVA) fiber with 1.2% oiling on the surface was used, and the mechanical and physical properties of which are presented in Table 3. The alkaline activator was a sodium-based silicate solution prepared by dissolving NaOH pellets (analytical grade, purity ≥98%)

and sodium silicate (Na₂O: 8.25 wt%, SiO₂: 27.50 wt%) in distilled water.

Five levels of silicate moduli (ratio of SiO₂ wt% to Na₂O wt%) of alkaline activator were considered for preparation of AASF matrices with a fixed binder combination of 50 wt% blast furnace slag and 50 wt% class F fly ash. The detailed mixture designs are shown in Table 4. In all mixtures, the w/b ratio and Na₂O content (in alkali activator with respect to total binder mass) were kept constant to be 0.32 and 4%, respectively. This w/b ratio was chosen to maintain adequate workability for all the paste mixtures. The mixtures were named M0.5, M0.8, M1.0, M1.2, and M1.5 accordingly, with the number representing the silicate modulus.

For sample preparation, the solid precursors were firstly dry mixed for 5 min using a HOBART® mixer at a low speed. Alkaline activator solution was then added gradually, and the batches were mixed for an additional 5 min at a medium speed. The fresh pastes mixtures were cast in a specially made mould for fiber pullout tests and small polyethylene vessels for ESEM/EDX analysis. The cast samples were further compacted with a vibration table before finally sealed with a plastic foil. After 1 day, the samples were demolded and were cured in a climate room (20 °C and ≥98% RH) until 28 days before testing.

2.2.2. ESEM/EDX characterization

Chemical compositions of reaction products in AASF matrices and within the fiber/matrix interfacial transition zone (ITZ) were characterized by environmental scanning electron microscopy (ESEM) and energy dispersive X-ray (EDX) analysis, using a Philips-XL30-ESEM equipped with Thermofisher UltraDry EDX detector. All

Table 3
Physical and mechanical properties of PVA fiber.

Fiber	Diameter (μm)	Density (g/cm³)	Strength (MPa)	Young's modulus (GPa)
PVA	40 and 300	1.30	1640	41.1

Table 4
Mixture design of AASF matrix.

Mixture	Slag (wt %)	Fly ash (wt %)	w/b ratio	Na₂O (wt %)	Silicate modulus
M0.5	50	50	0.32	4	0.5
M0.8					0.8
M1.0					1.0
M1.2					1.2
M1.5					1.5

Table 2
Chemical compositions and properties of raw materials.

Oxide (wt%)	SiO₂	Al₂O₃	Fe₂O₃	CaO	MgO	SO₃	Na₂O	K₂O	LOI	Fineness, % passing 45 μm
Slag	32.91	11.84	0.46	40.96	9.23	1.60	–	0.33	1.15	95
Fly ash	52.90	26.96	6.60	4.36	1.50	0.73	0.17	–	3.37	81

characterizations on the matrix and ITZ were conducted using paste samples at 28 days. Mixtures including M0.5-M1.5 were used for the characterization of reaction product composition in AASF matrices. For the interface characterization on element distribution within ITZ around PVA fiber, only the M1.0 specimen was used as a representative example. The samples were prepared following the method for single fiber pullout tests as described in Section 2.2.2, It is important to note that PVA fiber with a diameter of 300 μm was used for better clarification of fiber/matrix interface as well as ITZ.

EDX analysis of flat-polished samples is used to determine the phase assemblage in AASF matrices [59,60]. The reaction of investigated samples was stopped by solvent exchange using isopropanol followed by low vacuum drying. Before ESEM analysis, the samples were then impregnated using low viscosity epoxy resin and polished down to 0.25 um. The polished samples were examined for the observations of microstructure and backscattered electron (BSE) images were taken at an accelerating voltage of 15 kV. Additionally, the polished samples were carbon-coated before EDX measurement under high vacuum mode. The analysis was performed on the chemical compositions of the reaction products in AASF matrices and those around PVA fiber. Both spot analysis and line analysis were carried out. It should be noted that the atomic number, absorption, and fluorescence (ZAF) corrections were made in each EDX measurement, which is an implemented function in the Pathfinder software. ZAF corrections could convert apparent concentrations (raw intensities) into corrected concentrations to eliminate inter-element matrix effects, which makes it possible for semi-quantitative comparisons of element ratios.

2.2.3. Single-fiber pullout test

The adhesion properties of PVA fiber in M0.5-M1.5 AASF matrices were experimentally tested by single-fiber pullout tests following Redon et al. [28]. A mould with two-layer polyethylene bricks developed by Katz and Li [61] was used for casting as shown in Fig. 3 (a). A filament-type PVA fiber with a diameter of 40 μm was first cut, aligned, and fixed onto the bottom layer block using double-sided tape. Afterwards, the fibers were allowed for embedment into the matrices during the casting of fresh mixtures. The samples were put on a vibration table to remove entrapped air before sealing with plastic wrap. After 24 h, the samples were demolded and transferred to a climate room (20 °C and 95% RH) until 28 days. At 28 days, the hardened samples were cut into very thin specimens using a low-speed saw (Minitom, Struers) with fiber extruded out from one side (see Fig. 3 (b)). The embedded length (L_e) of PVA fiber was controlled to be around 1 mm to avoid fiber rupture while providing enough information for the bonding behavior during the pullout.

A micro tension-compression testing device (Kammrath & Weiss) shown in Fig. 4 (a) was used for single-fiber pullout tests. Both the surface of the thin specimen and the free end of the PVA fibers were glued to two small metal blocks. Afterwards, they were mounted on the testing device using two metal blocks, which were fixed to an actuator and a load cell. A 10 lb. (44.48 N) load cell was included in the system for pullout load testing with an accuracy of 0.1%. Displacement controlled pullout was used with a constant displacement rate of 0.01 mm/s. At least 20 tests were conducted for each matrix.
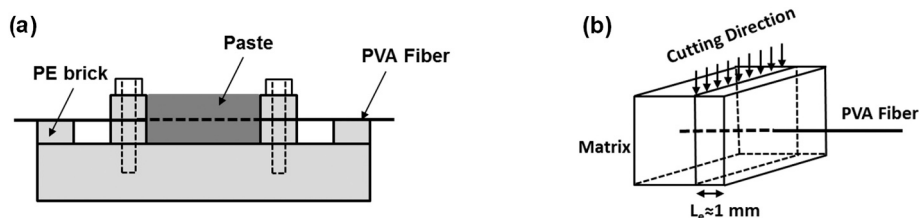
3. Results and discussions

3.1. Coordination of PVA to Ca and Na

The radial distribution functions (RDFs) of Ca and Na ions with the oxygen atoms from PVA molecules and their respective CNs for the composites with the considered Ca/(Si+Al) and Al/Si ratios are shown in Fig. 5. The coordination to the cations from the C-(N-)A-S-H surface can be related to the formation of electrostatic forces between the PVA molecules and the C-(N-)A-S-H gel.

As shown in Fig. 5, these plots show sharp peaks at distances around 2.0 Å and 2.2 Å for the RDFs of Na-O_{PVA} and Ca-O_{PVA}, respectively. These peaks correspond to the first coordination shell of the oxygen atoms of the PVA to the cations from C-(N-)A-S-H gel and consequently to the Ca-O_{PVA} and Na-O_{PVA} distances. It must be noted that neither the Ca/(Si+Al) ratio nor the Al/Si ratio affects Na-O_{PVA} and Ca-O_{PVA} distances. Nevertheless, as the Ca/(Si+Al) ratio increases from 0.75 to 1.2, the coordination of the PVA molecules to Ca ions grows progressively from 0.03 to 0.43 Ca ions per oxygen atom as a consequence of the higher Ca content. The increasing coordination to Ca ions provokes a slight decrease in the coordination of the oxygen atoms to the Na ions as the Ca/(Si+Al) ratio rises. This is because Ca is a divalent cation that can establish stronger electrostatic interactions with the negative charged functional groups of the PVA fiber and can displace the Na ions. It should be noted that the Ca/(Si+Al) ratio of 0.5 relates to the complete replacement of the interlaminar Ca by Na. This replacement (1 Ca^{2+} by 2 Na$^+$) results in much higher Na content than in the other systems, explaining the high Na-O_{PVA} coordination for that system. Regarding the effect of the Al/Si ratio, the CNs reveals that the coordination of PVA to Na is increased significantly due to the larger amount of Na at high Al/Si ratios. This can be better visualized in Fig. 6, which compares the values of the CNs for Ca and Na to the oxygen atoms of the PVA molecules at the studied Ca/(Si+Al) and Al/Si ratios.

The large capacity of the PVA fiber to coordinate with cationic species suggests that the incorporation of these polymers to the C-(N-)A-S-H gel may help to increase the Ca and Na content during the reaction. This behavior was analyzed by performing an *in situ* polymerization of the C-(N-)A-S-H gel in presence of a PVA fiber as shown in Fig. 7 (a). It should be noted that the precursors are present in the appropriate proportion to reach the average Ca/(Si+Al) ratio of 1.3 and the Al/Si ratio of 0.5. The Ca/(Si+Al) ratio is monitored as a function of the distance to the PVA fibers (see Fig. 7 (b)), computing the pair distribution function of those ratios around the oxygen atoms from PVA molecules. Here, the Ca/(Si+Al) ratio is significantly higher around the PVA fibers than the average (1.3), suggesting that the incorporation of PVA during the synthesis of the C-(N-)A-S-H gel may result in higher Ca/(Si+Al) ratios.

3.2. Coordination of PVA to the C-(N-)A-S-H surface

Besides the interaction of the PVA fibers with the C-(N-)A-S-H gel through the Ca and Na cations from the surface, the formation of hydrogen bonds is also possible between the hydroxyl groups of the PVA molecules and the oxygen atoms from the surface. The RDFs and CNs of H atoms of the hydroxyl groups in PVA fibers to the oxygen atoms of the C-(N-)A-S-H surface are plotted in Fig. 8, which can be used to
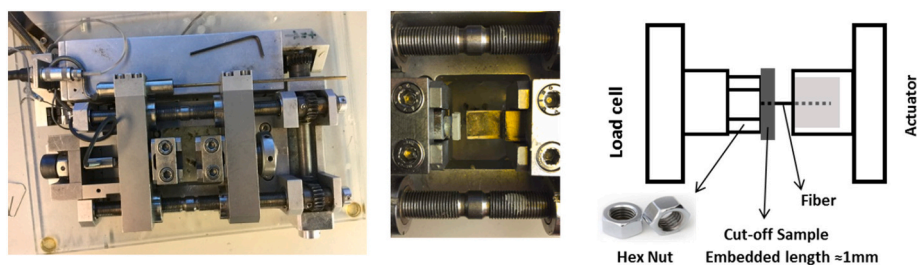

Fig. 3. Pullout sample preparation methods: (a) casting and (b) precise cutting.

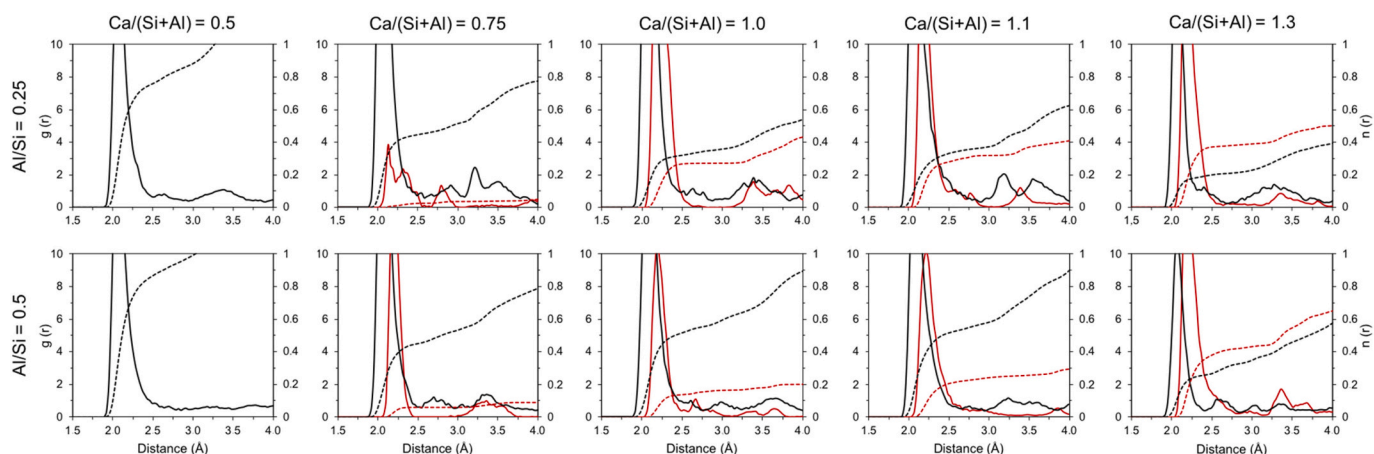**Fig. 4.** Experimental setup of the single-fiber pullout test [25].

Fig. 5. Radial distribution functions (continuous lines) and coordination numbers (dashed lines) for Na-O_{PVA} (in black) and Ca-O_{PVA} (in red) for the C-(N-)A-S-H gel with Ca/(Si + Al) ratios of 0.5, 0.75, 1.0, 1.1 and 1.3 at Al/Si ratios of 0.25 and 0.5.
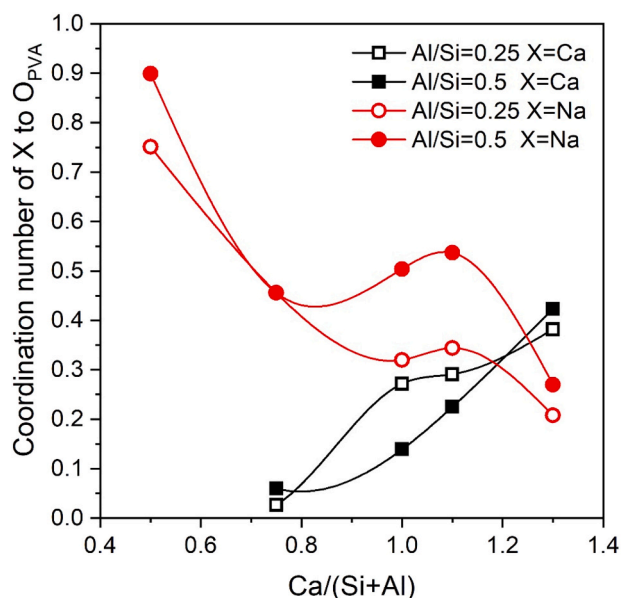

Fig. 6. Coordination numbers of Na (in red) and Ca (in black) to the oxygen atoms of PVA molecules for the studied PVA/C-(N-)A-S-H composites.

investigate the formation of hydrogen bonds between the polymer and the matrix [33].

It is observed that the main peak of the RDFs is around 1.8 Å, which matches the characteristic distance between the donor H atoms and the acceptor O atoms in hydrogen bonds [62,63]. As shown in Fig. 9, the CNs reveal that the coordination between the donor H from the PVA fibers and the acceptor O atoms from the surface decreases as the Ca/

(Si+Al) ratio increases and the Al/Si ratio decreases, suggesting that there is a higher number of hydrogen bonds between the PVA molecules and the C-(N-)A-S-H gel at low Ca/(Si+Al) ratios and high Al/Si ratios. The reduction at higher Ca/(Si+Al) ratios is attributed to the greater Ca content, which can prevent the formation of hydrogen bonds by coordinating to the hydroxyl groups, while the presence of Na ions does not hinder the formation of the hydrogen bonds between the PVA and the C-(N-)A-S-H surface, probably due to the smaller size and charge than those of Ca ions.

It is also essential to determine the angle of the hydrogen bonds between the hydroxyl groups of the PVA fibers and the oxygen atoms from the C-(N-)A-S-H surface since the strength of these bonds is strongly dependent on the bonding angle. The maximum strength is achieved when the three atoms involved in the hydrogen bond are aligned so that the donor H points directly to the acceptor electron pair [64]. To analyze the most probable distances and angles for hydrogen bonding in the PVA/C-(N-)A-S-H composites, a combined distribution function (CDF) of $H_{PVA}\cdots O_{C-(N-)A-S-H}$ distances and O_{PVA}-$H_{PVA}\cdots O_{C-(N-)A-S-H}$ angles was calculated and was illustrated in Fig. 10.

The CDF shown in Fig. 10 indicates that the most probable distance between donor hydrogen atoms and acceptor oxygen atoms from the C-(N-)A-S-H surface is around 1.8 Å, as seen in the RDFs, while the most probable angle defined by those atoms and the donor oxygen atom from PVA is between 145° and 165°, which indicate that they are not fully aligned. It is remarkable that despite the structural and chemical differences, the most probable distances and angles for the hydrogen bonds are in the same range for all the composites analyzed in this study.

3.3. Adhesion mechanism of PVA in C-(N-)A-S-H gel

The functional form of the potential energy in the force fields (CSHFF [52] and CHARMM [53] force fields) employed in the MD simulations in this study includes bond terms to describe the interactions of the atoms
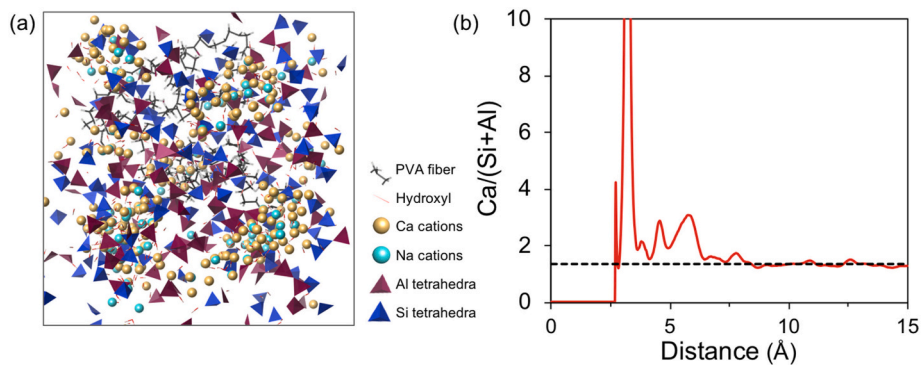
Fig. 7. (a) Snapshot of the *in situ* polymerization process of C-(N-)A-S-H gel around a PVA molecule in a simulation box with an average Ca/(Si+Al) of 1.3 and Al/Si ratio of 0.5. (b) Evolution of the Ca/(Si+Al) ratio as a function of the distance from the oxygen atoms of the PVA fibers. The black dashed indicates the average Ca/(Si+Al) ratio of 1.3.
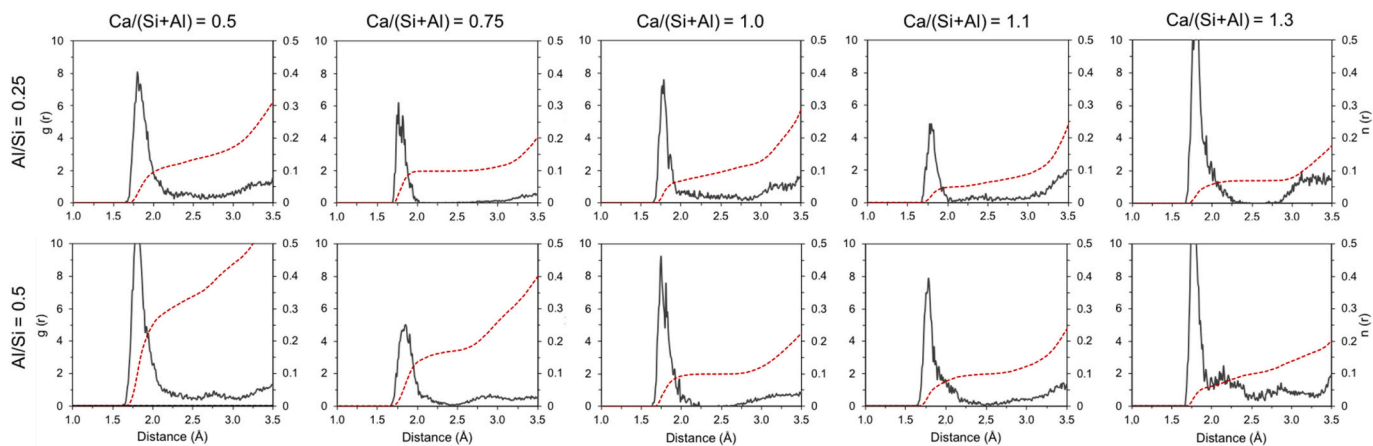

Fig. 8. Radial distribution functions (black continuous lines) and coordination numbers (red dashed lines) for H_{PVA}-$O_{C-(N-)A-S-H}$ with Ca/(Si+Al) ratios of 0.5, 0.75, 1.0, 1.1 and 1.3 at Al/Si ratios of 0.25 and 0.5.
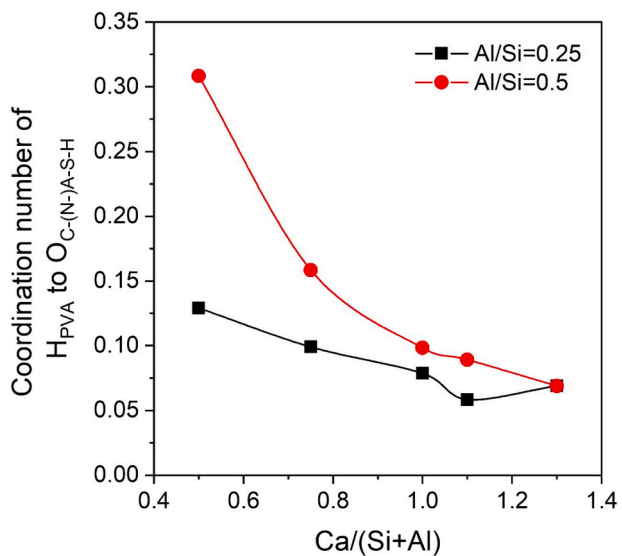
Fig. 9. Coordination numbers of donor hydrogen atoms from PVA fibers to the oxygen atoms of C-(N-)A-S-H surface for the studied PVA/C-(N-)A-S-H composites.
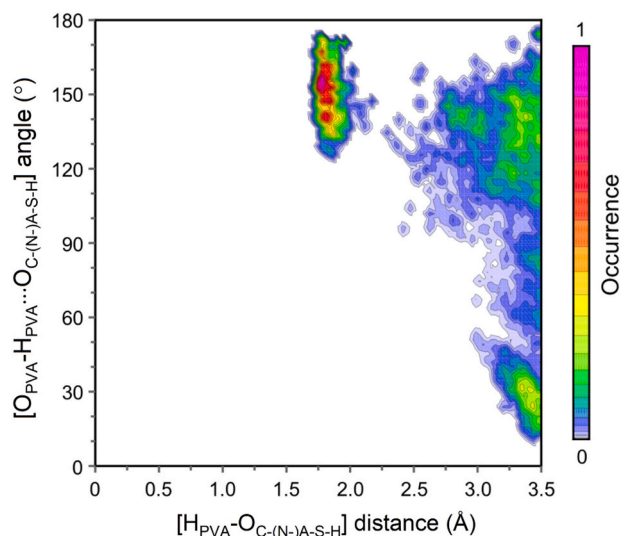
Fig. 10. Combine distribution function of hydrogen bond distances and angles between the PVA fibers and the C-(N-)A-S-H surfaces. Red colors correspond to the most probable configurations, while the blue ones are related to the less probable configurations.

linked by covalent bonds and non-bonded terms that describe the electrostatic interactions and the van der Waals forces between particles. Since the PVA molecules are not covalently linked to the C-(N-)A-S-H surface, the interaction between them is due to electrostatic and van der Waals interactions. The adsorption enthalpy of PVA fibers in C-(N-)A-S-H gel for the different Ca/(Si+Al) and Al/Si ratios can be determined as indicated in Eq. (3), which serves as an indicator for the adhesion property.

$$\Delta H_{ads} = \Delta H_{PVA/C-(N-)A-S-H} - \Delta H_{PVA} - \Delta H_{C-(N-)A-S-H} \qquad (3)$$

where $\Delta H_{PVA/C-(N-)A-S-H}$ is the enthalpy of the whole composite, ΔH_{PVA} is the enthalpy of the PVA fibers, and $\Delta H_{C-(N-)A-S-H}$ is the enthalpy corresponding to the C-(N-)A-S-H gel without PVA. According to this definition, the adsorption enthalpy of more negative values indicates stronger interaction between PVA and C-(N-)A-S-H gel and a more thermodynamically favorable state. The values of the adsorption enthalpy for the composites with different Ca/(Si+Al) ratios and Al/Si ratios of 0.25 and 0.5 are shown in Fig. 11 in different units (kJ/m^2 and kJ/g).

The adhesion of the PVA molecules within the C-(N-)A-S-H gel, as shown in Fig. 11, is more favorable as the Ca/(Si+Al) ratio rises regardless of the Al/Si ratio. This can be attributed to the higher Ca content as the Ca/(Si+Al) ratio increases, allowing the development of more electrostatic interactions between those cations and the PVA fibers, as illustrated in Fig. 6. Additionally, the stronger adsorption is observed with a lower Al/Si ratio, particularly when Ca/(Si+Al) is high (>1.0). The higher coordination of the PVA molecules to the Na cations at high Al/Si ratios may be responsible for the decrease in the adsorption strength, since the electrostatic interactions with Ca, a divalent cation, are much stronger than with Na, a monovalent cation.

In addition to the coordination of the PVA to the cations, there are also hydrogen bonds between the oxygen atoms from the C-(N-)A-S-H surface and the hydroxyl groups of the PVA fibers. Despite the lack of clear consensus on the nature of the hydrogen bonds, this study describes the hydrogen bonds as a sort of Van der Waals interactions and their contribution to the adsorption enthalpy could be estimated. To this effect, the enthalpy of a single hydrogen bond for the most probable $H_{PVA}\cdots O_{C-(N-)-A-S-H}$ distance of 1.8 Å and $O_{PVA}-H_{PVA}\cdots O_{C-(N-)-A-S-H}$ angle of 160° according to Fig. 10, and the value has been estimated to be -4.84 kcal mol^{-1}. Considering the number of H atoms from PVA coordinated to oxygen atoms from the C-(N-)A-S-H surface, the adsorption enthalpy due to the hydrogen bond network between the PVA and C-(N-)A-S-H gel can be estimated. As can be seen in Fig. 12, the values of these adsorption enthalpies in both unit (kJ/m^2 and kJ/g) are one order of

magnitude smaller in absolute terms and its contribution to the total adsorption enthalpy ranges from nearly 15% in the composite with Al/Si and Ca/(Si+Al) ratios of 0.5 and 0.5 to 1.3% at high Ca/(Si+Al) ratios. It is found that the contribution to adhesion of the hydrogen bond network decreases as the Ca/(Si+Al) ratio rises and the Al/Si ratio declines, in agreement with the number of hydrogen bonds estimated in the previous section. Therefore, the contribution to the adhesion of the hydrogen bonds is only significant at low Ca/(Si+Al) ratios when the ionic concentration in the interlaminar space is low. At high Ca/(Si+Al) ratios, the adsorption mechanism of the PVA fibers in the C-(N-)A-S-H gel is almost exclusively electrostatic.

3.4. Experimental evidence

Experimental characterization was performed to provide further evidence of the adhesion properties and adhesion mechanism between PVA fiber and AASF matrix in addition to the MD simulations.

3.4.1. Chemical composition of AASF matrices

As indicated by the MD simulation, the chemical composition of C-(N-)A-S-H gel has a predominant influence on the adhesion properties between PVA fiber and AASF matrices. Hence, EDX point analysis was carried out on M0.5-M1.5 at 28 days to confirm the chemical nature of the main reaction product in AASF matrices. These points were selected carefully within the binder region, keeping sufficient distance from the unreacted particles [65]. A total of 80 to 90 measurements have been conducted for each AASF matrix. The microstructure of all AASF by BSE imaging tends to be quite similar and only one representative BSE image of the M1.0 matrix is shown in Fig. 13 (a). The binder region in darker grey color has a grey level between that of slag and fly ash and demonstrates a quite homogenous formation of reaction products and a dense microstructure with very limited capillary pores in black color. Additionally, the CaO-SiO$_2$-Al$_2$O$_3$ ternary diagram is plotted in Fig. 13 (b), in which Ca, Al, and Si are normalized to 100% on an oxide basis. Similar to [39], the experimental EDX data of all AASF matrices fall well in the region of AAS [66–68] as well as AASF [12–14,69–72], which again confirms the formation of C-(N-)A-S-H gel as the main reaction product in AASF paste. Also, the chemical compositions of the five C-(N-)A-S-H models for MD simulation are illustrated in the ternary diagram. It could be observed that the selected Ca/(Si+Al) and Al/Si ratios for C-(N-)A-S-H models provide a good estimation of the experimental data of all AASF matrices, particularly under low Ca/(Si+Al) ratios.

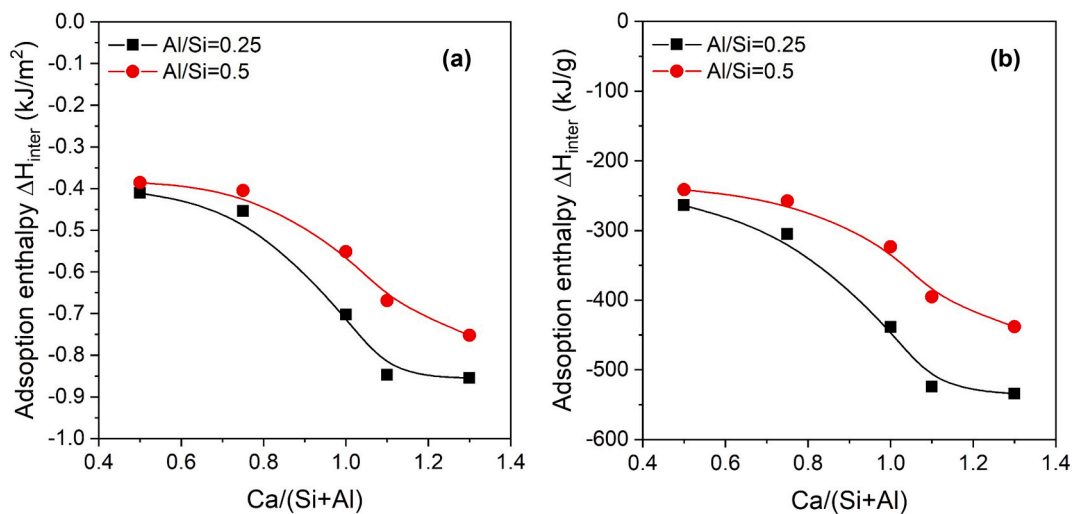To further evaluate the consistency between the chemical

Fig. 11. Adsorption enthalpies in (a) kJ/m^2 and (b) kJ/g of PVA molecules for the composites with Al/Si ratio of 0.25 (black squares) and 0.5 (red dots) at the considered theoretical Ca/(Si+Al) ratios.
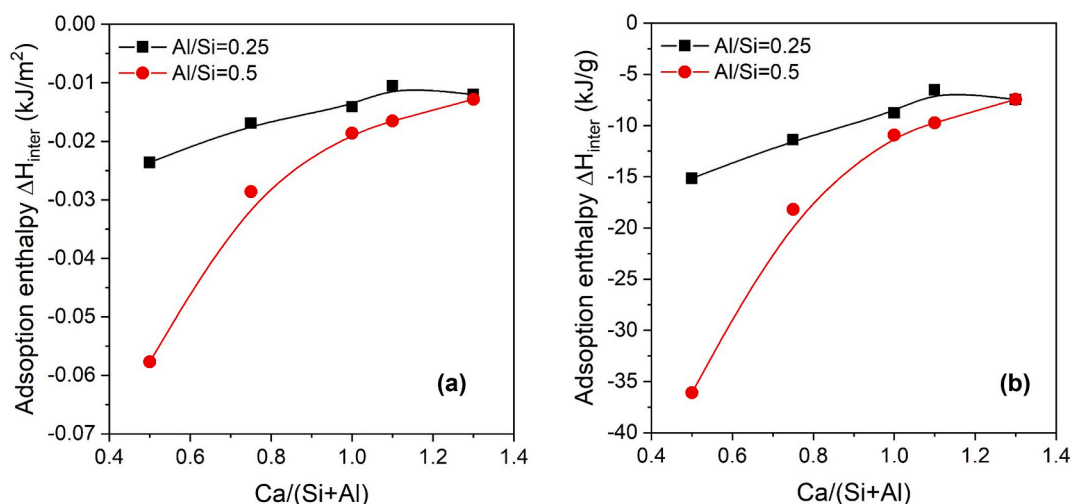
Fig. 12. Adsorption enthalpies in (a) kJ/m² and (b) kJ/g attributed to the hydrogen bonds between the PVA molecules and the C-(N-)A-S-H gel for the composites with Al/Si ratio of 0.25 (black squares) and 0.5 (red dots) at the considered theoretical Ca/(Si+Al) ratios.
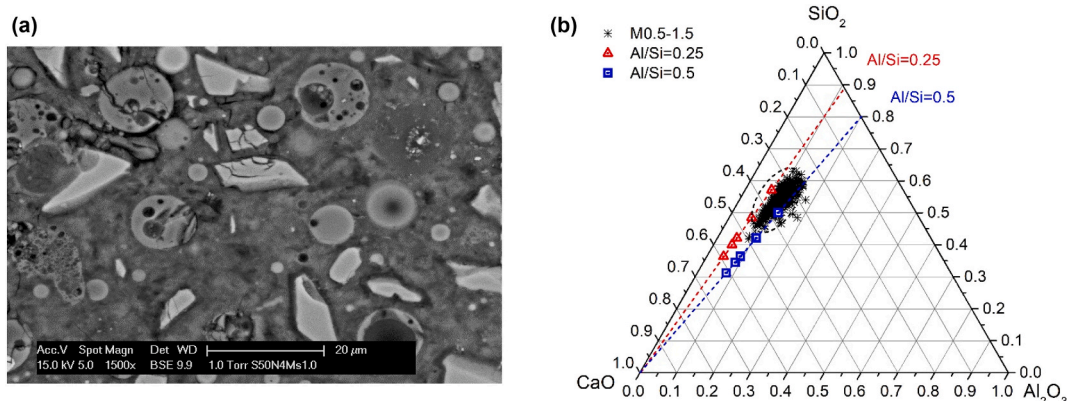

Fig. 13. (a) Representative BSE images of M1.0 AASF matrix and (b) ternary diagram of CaO-SiO₂-Al₂O₃ of EDX spot analysis for reaction product in the M0.5-M1.5 AASF matrices and C-(N-)A-S-H model for MD simulation (Al/Si = 0.25 and Al/Si = 0.5).

composition of C-(N-)A-S-H gel between the MD simulations and experiments, the Ca/(Si+Al) and the Al/Si ratios of the C-(N-)A-S-H gel in M0.5-M1.5 matrices are shown in Fig. 14 (a) and (b), respectively. With increasing activator silicate modulus (M0.5-M1.5), the Ca/(Si+Al) ratio declines whereas this influence on the Al/Si ratio is insignificant. Besides, the histogram of both atomic ratios shown in Fig. 14 (c) and (d) is also fitted with the simple Gaussian curve with the minimization of the least-squares using Origin Software. The characteristics of the fitted Gaussian distribution are thus characterized by its mean of the distribution (μ) and its standard deviations (STDs, or σ). According to the central limit theorem in statistics, the well-fitted Ca/(Si+Al) and Al/Si ratios indicate that the results are influenced by a large number of independent random variables. In this case, they could be different experimental errors induced by either the random error of the equipment and procedures, or the intermixing of multiple phases within reaction products. Most likely, the influence is due to the acquisition of information from an "interaction volume" within an EDX spot analysis. Under the acceleration voltage of 15 kV, the interaction volume has a radius of approximately 1.0–2.5 μm into the sample surface when this major reaction product is C-(N-)A-S-H gel [73], which causes intermixed analysis of phases.

Although the mean of the distribution (μ) in each of the ratios could reasonably reflect the chemical composition of the intermixed phases, it cannot properly describe the true chemical composition of "pure" C-(N-)A-S-H gel. Considering the presence of remnant fly ash particles and

unreacted silicate-based activator within the matrix, the intermixing is often towards Si-rich phases, which could lead to underestimation of the true Ca/(Si+Al) ratio. In contrast, the true Al/Si is possibly overestimated considering the higher Al/Si ratio (0.60) of fly ash. As a result, the higher end value of Ca/(Si+Al) ratio (μ+2σ) and the lower end value of Al/Si ratio (μ−2σ) are selected to reflect the chemical composition following previous studies on C-A-S-H gel [59]. Notably, they correspond to the value at 95% level and 5% level of the Ca/(Si+Al) ratio and Al/Si ratio in its Gaussian distribution, respectively. These proposed chemical compositions of "pure" C-(N-)A-S-H gel determined experimentally along with the five C-(N-)A-S-H models for MD simulation are again plotted in the CaO-SiO₂-Al₂O₃ ternary diagram in Fig. 15. The grey-colored area constructed by the tie lines corresponds to the chemical compositions of the C-(N-)A-S-H gel covered by the MD simulation. It is evident that the proposed chemical composition of "pure" C-(N-)A-S-H gel with Ca/(Si+Al) ratio of 0.50–0.69 and Al/Si ratio of 0.30–0.36 fall well into the grey areas, which confirms the consistency between the C-(N-)A-S-H gel formed in M0.5-M1.5 AASF matrices and the C-(N-)A-S-H model for MD simulation. Consequently, the C-(N-)A-S-H model (Section 2.1.2) can reasonably represent the realistic C-(N-)A-S-H gel as the main reaction product in AASF matrices. Besides, the reliability of using these models as the basis for MD simulation is further substantiated.

3.4.2. Element distribution around PVA fiber

The influence of PVA fiber on the reaction products and the spatial
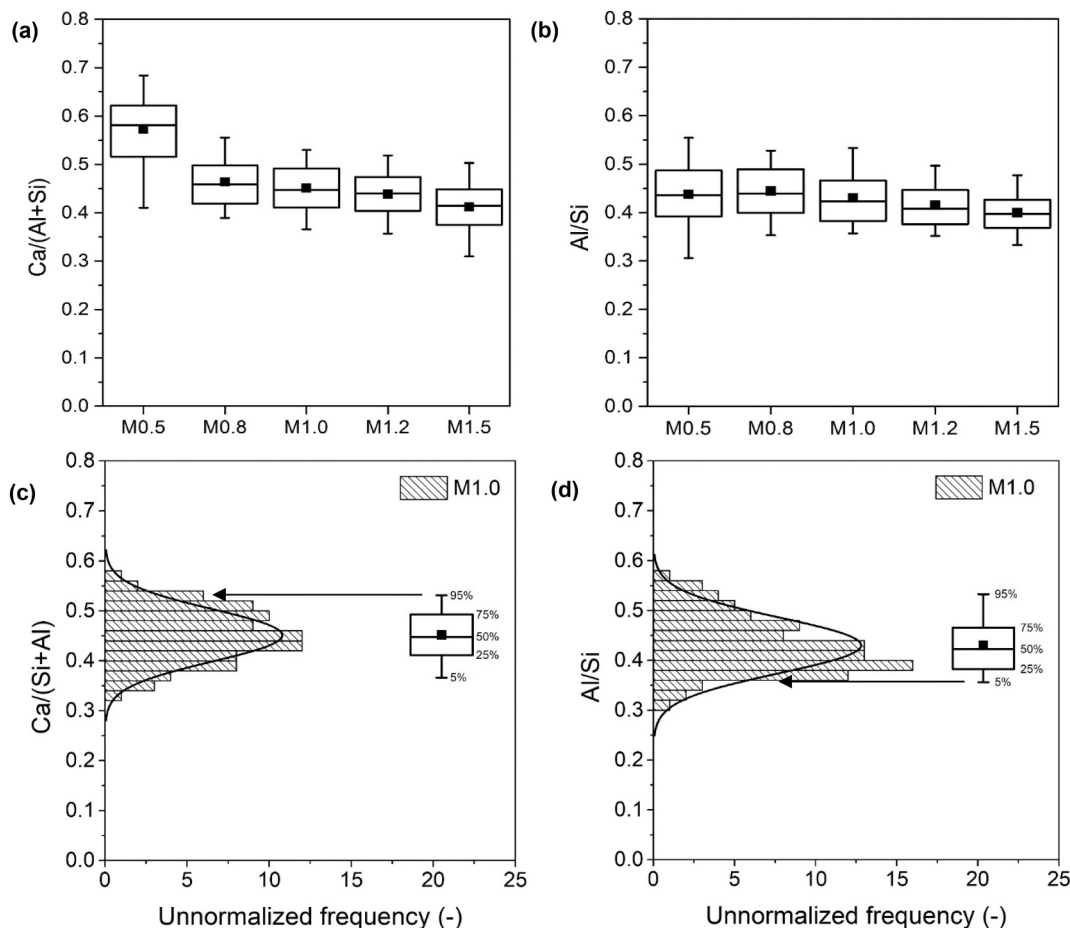
Fig. 14. Box plot of (a) Ca/(Si+Al) ratio and (b) Al/Si ratio of the main reaction products in AASF M0.5-M1.5 matrices; Representative histogram of EDX data points (c) Ca/(Si+Al) ratio and (d) Al/Si ratio of the main reaction products in AASF M1.0 Matrix. The median value (-), the mean value (■), the values at 25%, and 75% (box edges), and the values at 5% and 95% (whiskers) are illustrated.
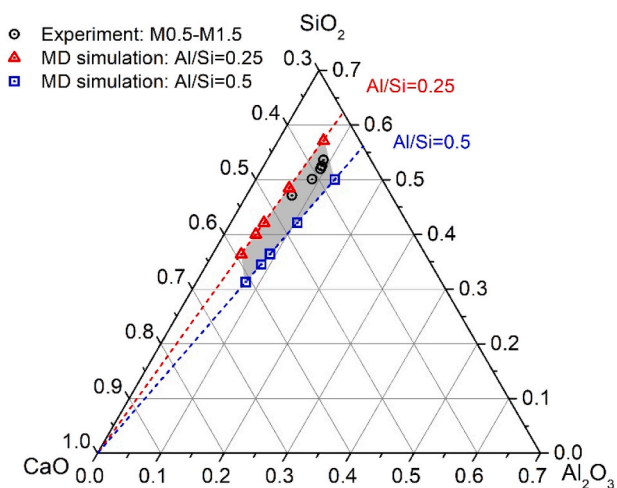

Fig. 15. The CaO-SiO$_2$-Al$_2$O$_3$ ternary diagram of the chemical composition of "pure" C-(N-)A-S-H gel in the M0.5-M1.5 AASF matrices and C-(N-)A-S-H model for MD simulation (Al/Si = 0.25 and Al/Si = 0.5).

distribution of elements in the ITZ were studied by EDX element mapping and spot analysis on the reaction products in ITZ formed around PVA fiber. Fig. 16 illustrates EDX element mapping (Na, Mg, Al, Si, and Ca in atomic %) of the reaction products around PVA fiber. The higher brightness in the map represents the atomic concentration of certain

elements regardless of different colors. As shown in Fig. 16, the correlation between Al and Si could be observed in fly ash particles. Slag particles, rich in Ca and Mg content, show a more homogenous Ca and Mg distribution. More significantly, the Ca map depicts a rim of reaction products with high brightness around PVA fiber, which distinguished itself from the dominant C-(N-)A-S-H gel in median brightness within the AASF matrix. This indicates the formation of a Ca-rich reaction product near the fiber/matrix interface in comparison to the reaction products away from PVA fiber. Notably, other elements including Na, Mg, Al, and Si, on the other hand, do not show preferential space distribution due to the presence of PVA fiber.

The EDX spot analysis in the ITZ between fiber and matrix was conducted to further determine the detailed chemical nature of the reaction products and the results are presented in a CaO-SiO$_2$-Al$_2$O$_3$ ternary diagram in Fig. 17 (a). Except for the evident increase of Ca, the reaction product in the ITZ has at least a similar Al/Si ratio in comparison with the one in the matrix. On the contrary, the related Ca/(Si+Al) ratio (1.44) is considerably higher than that in the matrix (0.53). Fig. 17 (b) gives the representative EDX spectra for both reaction products. Considering the similarity between the two EDX patterns, the reaction product formed within ITZ near the PVA fiber is believed to be a kind of Ca-rich C-(N-)A-S-H gel to be distinguished from the C-(N-)A-S-H gel formed in AASF matrix. Another possibility relates to the formation of a portlandite (CH) layer at the PVA fiber surface, which was reported in previous studies concerning PVA fiber reinforced cementitious composite. The adhesion properties of PVA fiber in the cementitious matrix are also believed to be closely related to the CH layer in the ITZ [30,74]. The formation of CH in the AASF system is highly unlikely at ambient
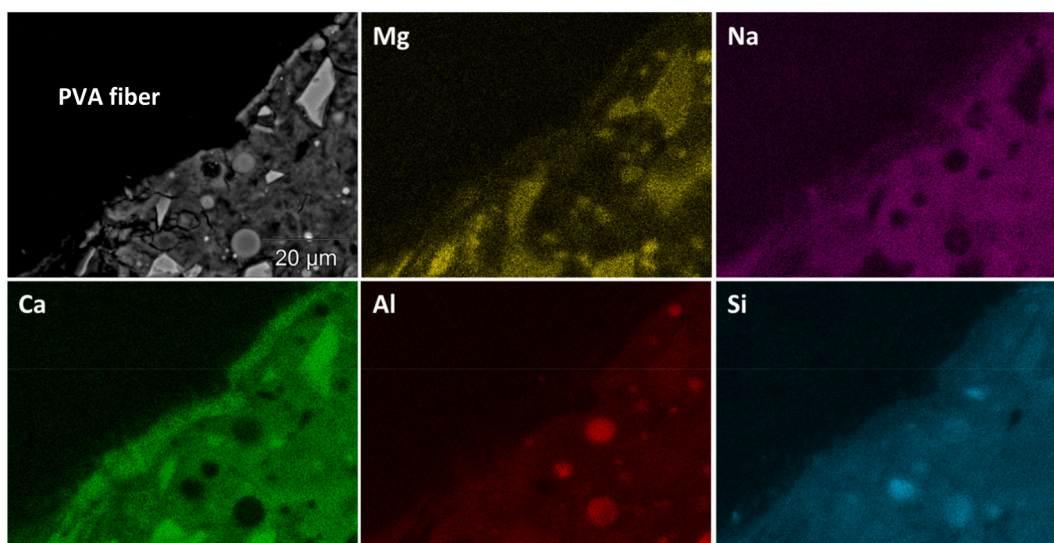
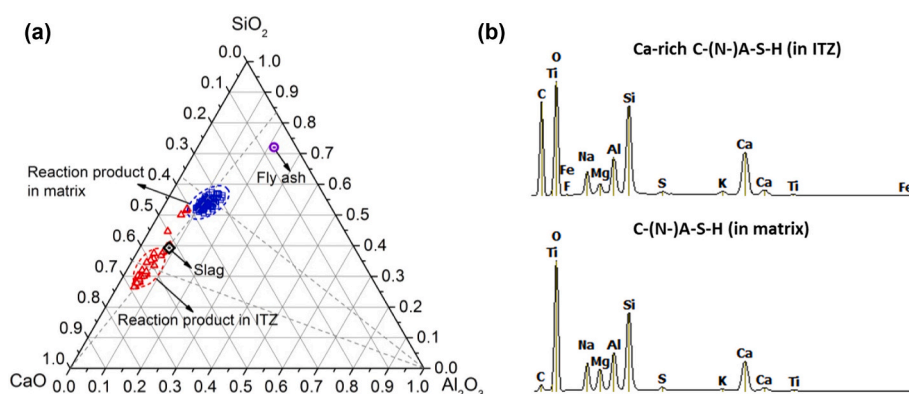**Fig. 16.** EDX element mapping (Na, Mg, Al, Si, and Ca in atomic %) of reaction products around PVA fiber.

Fig. 17. (a) Ternary diagram of CaO-SiO_2-Al_2O_3 of EDX spot analysis for reaction product in the matric and around PVA fiber (b) representative EDX spectra of Ca-rich C-(N-)A-S-H gel and C-(N-)A-S-H gel.

temperature since the solubility product K_{sp} of CH is much higher than of C-(N-)A-S-H gel [75]. In this case, the preferential formation of the amorphous C-(N-)A-S-H gel will be dominating the reaction process over the formation of crystalline phases as predicted by thermodynamics modeling [42,76]. This evidence also effectively precludes the possibility of the intermixing of C-(N-)A-S-H gel with CH. In fact, the main reaction products of sodium silicate-based AASF is reported to be amorphous [12,71,77] and seldom has new crystalline phases except for hydrotalcite has been reported.

Additionally, to reveal the influence of PVA fiber on the elemental space distribution and element ratios of reaction products within ITZ, carefully selected EDX Line scans from an AASF matrix to the PVA fiber were performed to avoid visible unreacted slag and fly ash. The chemical compositions in terms of atomic percentage of Na, Mg, Al, Si, and Ca are plotted representatively in Fig. 18. As demonstrated, the concentration of elements including Na, Mg, Al, Si decrease progressively from the ITZ to the PVA fiber region. Some fluctuations of element concentrations are detected within the ITZ, which is due to the heterogeneous characteristics of the AASF matrix. Particularly, a substantial decline of Si along the line into the PVA fiber region is observed, indicating the reaction products within ITZ is also dominated by Si content along with Ca. On the other hand, the concentration of Ca experiences a marked increase within ITZ before its continuous decrease into the fiber region. Furthermore, the corresponding atomic ratio of Ca/Si and Ca/(Si+Al) are also plotted in Fig. 18. Both element ratios significantly increase

within the ITZ and reach maximum precisely at the fiber/matrix interface. All these above-mentioned findings are well in line with the EDX spot analysis indicating Ca-rich reaction products at the ITZ. Additionally, the relatively stable Mg concentration within ITZ precludes the contribution of extra Ca by the unreacted slag in the EDX analysis. Notably, it also indicates the presence of PVA fiber has no significant influence on the Mg distribution or the related formation of hydrotalcite, which was detected to be strongly intermixed with the C-(N-)A-S-H gel [78]. Thus, the hypothesis of Ca-rich C-(N-)A-S-H gel formation at the fiber/matrix interface is further justified.

These results from EDX coincide well with the MD simulation results of RDF and CNs of Ca, Si, Al to O_{PVA} as well as the *in situ* polymerization results (Section 3.1), which all indicate a strong affinity of Ca^{2+} cation and weak interaction of Si and Al to PVA fiber. This is significant since it serves as experimental evidence that the inclusion of PVA fiber into the AASF matrix could have a non-negligible impact on the formation of reaction products at least in the ITZ. This could be the reason for the differences found between G_d of PVA fiber in AAMs systems and cementitious systems [23–25]. Furthermore, this effect leading to the formation of Ca-rich C-(N-)A-S-H gel in the ITZ will have considerable influence on the adhesion properties and is thereby essential for interface modification for high-performance alkali-activated composite based on AASF. Finally, unlike those of Ca, the RDF and CN of Na to O_{PVA} shows no strong affinity around PVA fiber, which could be due to the very abundant concentration of Na in the pore solution throughout the
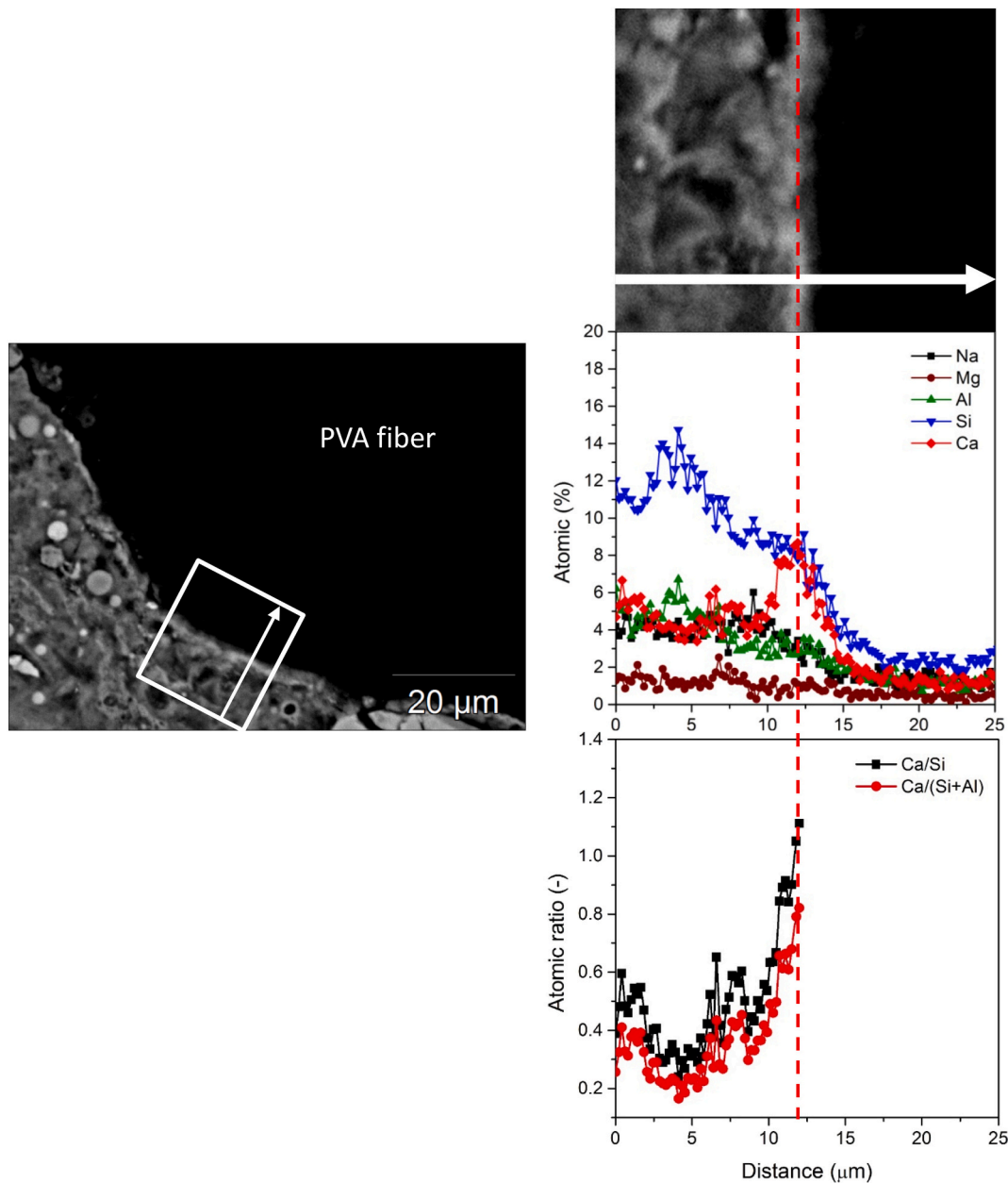
Fig. 18. Elemental distributions of Na, Mg, Al, Si, Ca, and Ca/(Si+Al) ratios of the reaction products in the ITZ.

formation of C-(N-)A-S-H gel in the AASF matrix [79].

3.4.3. Chemical bonding energy between PVA fiber and AASF matrix

The single-fiber pullout load-displacement curves of PVA fibers embedded in the M1.0 AASF matrix are shown in Fig. 19 (a). The general profile of a single-fiber pullout curve can be decomposed into three main regimes [28]. Initially, a stable fiber debonding process occurs along the fiber/matrix interface. The load resisted by the fiber is increasing up to P_a when the debonded length L_d equals the fiber embedded length L_e. The fiber was then fully debonded but the embedded fiber end was not yet moving. At this point, the displacements were only contributed by the elastic stretching of the debonded fiber segment and the free length. The sudden load decrease from P_a to P_b corresponds to the chemical bonding energy (G_d). Finally, the fiber starts to slip in the slippage phase, in which the pullout is resisted by frictional forces. The fiber undergoes sliding with an evident slip-hardening effect, characterized by the coefficient β ($\beta>0$) [80]. Slip-hardening occurs due to their lower rigidness in comparison to the surrounding matrix. The accumulated

damages on the fiber surface could induce a so-called 'jamming' effect, which leads to an increasing fiber pullout resistance.

The adhesion between PVA fiber and the AASF matrix was quantified based on single-fiber pullout tests. The debonding process during the fiber pullout is assumed to be a tunnel crack propagation along the fiber/matrix interface, which is resisted by the debonding fracture energy [81]. This assumed fracture energy is also widely known as the chemical bonding energy G_d between PVA fiber and matrix and could be calculated using Eq. (4) [28].

$$G_d = \frac{2(P_a - P_b)^2}{\pi^2 E_f d_f^3} \tag{4}$$

where E_f, d_f, and L_e are the elastic modulus, diameter, and embedded length of the PVA fiber, respectively. P_a is the load up to full debonded length (debonded length L_d=embedded length L_e) and P_b is the load when the fiber begins to slip.

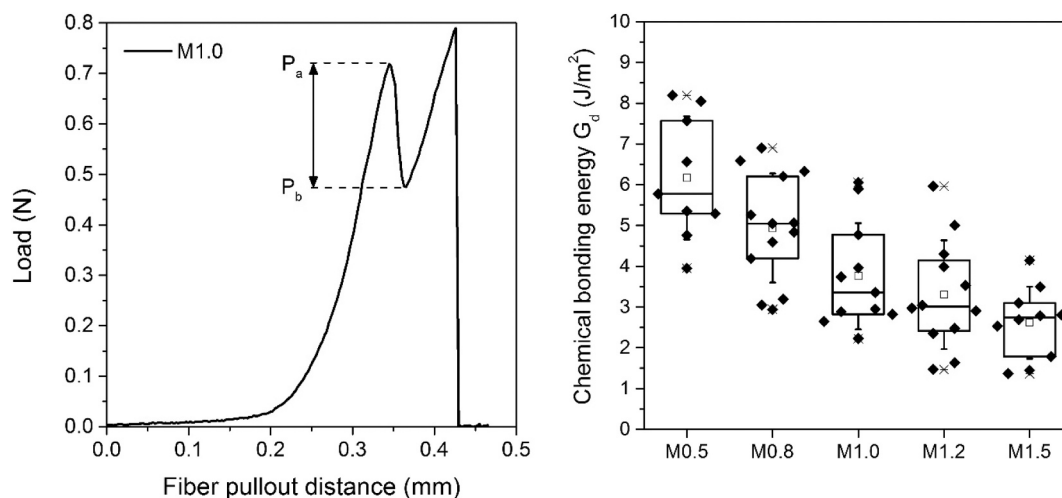The G_d of PVA in M0.5-M1.5 AASF matrices in box plots are

Fig. 19. (a) Representative single-fiber pullout curves of PVA fiber in M1.0 AASF matrix; (b) Chemical bonding energy (G_d) of PVA fiber in M0.5-M1.5 AASF matrices determined from at least 16 measurements. The box plot illustrates the median value (-), the mean (□), the values at 25% and 75% (box edges), and the standard deviation (whiskers).

summarized in Fig. 19 (b). Each of the box plots is derived from at least 16 individual pullout tests. It is worth noting that relatively large standard deviations (STD) have been observed for G_d, which can be the result of an inhomogeneous distribution of reaction products around PVA fibers. Previous studies on interface properties using single-fiber pullout tests also present quite large STDs [23–25]. Therefore, the data is considered reliable as long as the trend of influencing factors could be revealed. A clear trend of the average value of G_d could be found in Fig. 19 (b), which decreases from 6.2 to 2.9 J/m^2 with increasing activator silicate modulus from 0.5 to 1.5. By increasing the silicate modulus, more available silica species were introduced into the matrix and consequently changed the global reaction and chemical nature of the reaction products [66,82,83], which is reflected by the decreasing Ca/(Si+Al) ratio. Therefore, G_d is positively correlated with the Ca/(Si+Al) ratio of the C-(N-)A-S-H gel in matrices. This trend is compared with the MD simulation results and is depicted in Fig. 20. It is clearly shown that experimentally attained G_d as a function of Ca/(Si+Al) is well in line with the MD simulation results on the adsorption enthalpy, which also rises primarily with increasing Ca/(Si+Al) ratio of

the C-(N-)A-S-H model. Compared with Al/Si ratio, the Ca/(Si+Al) ratio plays a more dominant role in determining the adhesion properties, which also agrees well with the MD simulation results suggesting that the favored absorption at a lower Al/Si ratio is only significant at high Ca/(Si+Al) ratio.

Notably, the simulated adhesion enthalpy and the G_d as adhesion property also present a certain gap with a difference in magnitude of 100 times regardless of the Al/Si ratio of C-(N-)A-S-H gel used for MD simulation. Since the G_d acquired experimentally relates to an effective bonding energy per m^2, the difference between G_d and the one given by the MD simulation could be related to the effective surface coverage of C-(N-)A-S-H gel over the PVA fiber. It is important to note that the MD simulation considers saturation electrostatic interaction between Ca^{2+} to O$_{PVA}$, which despite the contribution of hydrogen bonding, has the main contribution to adhesion. However, the PVA fiber surface in reality is not fully occupied by C-(N-)A-S-H gel. The reason could be the heterogeneous distribution of reaction products. Specifically, a more porous ITZ on the fiber surface despite the minimized "wall effect" due to the small magnitude of fiber diameter [84,85] could decrease the effective coverage rate of reaction products on the fiber surface. Besides, the oiling treatment on the fiber surface hinders the coverage as well. All these factors contributed to a low rate of effective coverage of C-(N-)A-S-H gel over the PVA fiber, and thereby a lower experimental value of G_d in comparison to simulated ones. Furthermore, it seems that the difference between MD simulations and the experimental results could be also attributed to the disparities of length scale involved, similar to the size effect found in brittle materials like concrete [86]. Thus, the direct linking of adhesion properties in MD simulation to the mesoscale bonding G_d is only possible with essential upscaling processes.

Despite the difference in the magnitude of the adhesion properties, the consistency between experiment and MD simulation suggests that the reaction products chemistry of C-(N-)A-S-H gel predominantly affects the PVA/C-(N-)A-S-H adhesion properties. It is also confirmed that the interface property tailoring could be achieved by the proper mixture design of AASF. Particularly, this information is highly valuable for the development of future PVA-based SHGC, the performance of which is largely governed by the adhesion properties.

4. Conclusions

This work presents a combined approach using both molecular dynamics (MD) simulation and experimental characterization to investigate the adhesion mechanism, the interface nanostructure, and the
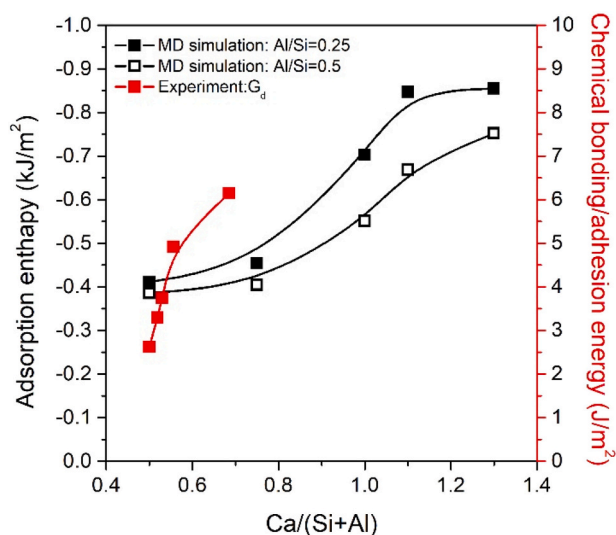

Fig. 20. Comparison between the experimentally attained chemical bonding energy G_d in AASF and the MD simulated adsorption enthalpy of PVA fiber in C-(N-)A-S-H gel.

related adhesion properties of PVA fiber to C-(N-)A-S-H gel as the main reaction product in alkali-activated slag/fly ash (AASF) matrix. Various Ca/(Si+Al) and Al/Si ratios of C-(N-)A-S-H gel were considered and their impacts on the adhesion energy and element space distribution within reaction products to PVA were simulated and experimentally verified. Based on the results and discussions of this study, the following conclusions can be drawn:

- The MD simulations indicate that the origin of adhesion between PVA and C-(N-)A-S-H gel at high Ca/(Si+Al) ratios (>1) is almost entirely due to the electrostatic interactions between the hydroxyl group in PVA and the Ca^{2+} and Na^+ ions within C-(N-)A-S-H gel, whereas the contribution to the adhesion due to the hydrogen bonding between PVA molecule and C-(N-)A-S-H gel is only considered significant at low Ca/(Si+Al) ratios (<1).
- The experimentally attained chemical bonding energy G_d of PVA fiber in AASF coincides well with the adsorption enthalpy of PVA in C-(N-)A-S-H gel calculated by MD simulation. Despite the differences in magnitude, the adhesion properties enhance primarily by increasing the Ca/(Si+Al) ratio of C-(N-)A-S-H gel.
- The polarity of the PVA molecule induced by the hydroxyl functional group and its interaction with C-(N-)A-S-H gel presents a high affinity of Ca and Na cations to PVA molecule, leading to a higher coordination number of Ca and Na to O_{PVA} in comparison to Si and Al. Accordingly, the formation of Ca-rich C-(N-)A-S-H gel with considerably higher Ca/(Si+Al) and similar Al/Si ratios were detected at the ITZ near the PVA fiber in comparison to those of the AASF matrix.
- The difference between the experimental attained chemical bonding energy G_d and simulated adsorption enthalpy relate to the effective coverage of C-(N-)A-S-H gel on the PVA fiber surface. Furthermore, it could also arise from the disparities of length scale involved, similar to the results of the size effect.
- The study provides further insights into the adhesion mechanism of PVA fiber to C-(N-)A-S-H gel formed in the AASF system and contributes to the tailoring strategies for composite performance enhancement through proper mixture design. These findings are particularly valuable for the development of future PVA-based strain-hardening geopolymer composite.

CRediT authorship contribution statement

Shizhe Zhang: Conceptualization, Methodology, Investigation, Formal analysis, Writing - Original Draft, Writing - Review & Editing Eduardo Duque-Redondo: Methodology, Investigation, Formal analysis, Writing - Original Draft, Writing - Review & Editing Albina Kostiuchenko: Methodology, Investigation, Writing - Review & Editing Jorge S. Dolado: Methodology, Supervision, Writing - Review & Editing Guang Ye: Supervision, Writing - Review & Editing, Project administration, Funding acquisition.

Declaration of competing interest

The authors declare that they have no known competing financial interests or personal relationships that could have appeared to influence the work reported in this paper.

Acknowledgments

References

[1] C. Shi, D. Roy, P. Krivenko, Alkali-activated Cements and Concretes, CRC press, 2006.

[2] J. Davidovits, Geopolymers, J. Therm. Anal. Calorim. 37 (1991) 1633–1656.

[3] J.L. Provis, S.A. Bernal, Geopolymers and related alkali-activated materials, Annu. Rev. Mater. Res. 44 (2014) 299–327.

[4] G. Habert, C. Ouellet-Plamondon, Recent update on the environmental impact of geopolymers, RILEM Tech. Lett. 1 (2016) 17–23.

[5] P. Duxson, J.L. Provis, G.C. Lukey, J.S. Van Deventer, The role of inorganic polymer technology in the development of 'green concrete', Cem. Concr. Res. 37 (2007) 1590–1597.

[6] K. Arbi, M. Nedeljkovic, Y. Zuo, G. Ye, A review on the durability of alkali-activated fly ash/slag systems: advances, issues, and perspectives, Ind. Eng. Chem. Res. 55 (2016) 5439–5453.

[7] M. Albitar, M.M. Ali, P. Visintin, M. Drechsler, Durability evaluation of geopolymer and conventional concretes, Constr. Build. Mater. 136 (2017) 374–385.

[8] F. Pacheco-Torgal, Z. Abdollahnejad, A. Camões, M. Jamshidi, Y. Ding, Durability of alkali-activated binders: a clear advantage over Portland cement or an unproven issue? Constr. Build. Mater. 30 (2012) 400–405.

[9] J. Zhang, C. Shi, Z. Zhang, Z. Ou, Durability of alkali-activated materials in aggressive environments: a review on recent studies, Constr. Build. Mater. 152 (2017) 598–613.

[10] J. Van Deventer, J. Provis, P. Duxson, G. Lukey, Reaction mechanisms in the geopolymeric conversion of inorganic waste to useful products, J. Hazard. Mater. 139 (2007) 506–513.

[11] P. Duxson, J.L. Provis, G.C. Lukey, J.S.J. van Deventer, The role of inorganic polymer technology in the development of 'green concrete', Cem. Concr. Res. 37 (2007) 1590–1597.

[12] I. Ismail, S.A. Bernal, J.L. Provis, R. San Nicolas, S. Hamdan, J.S. van Deventer, Modification of phase evolution in alkali-activated blast furnace slag by the incorporation of fly ash, Cem. Concr. Compos. 45 (2014) 125–135.

[13] F. Puertas, A. Fernández-Jiménez, Mineralogical and microstructural characterisation of alkali-activated fly ash/slag pastes, Cem. Concr. Compos. 25 (2003) 287–292.

[14] N.K. Lee, H.K. Lee, Reactivity and reaction products of alkali-activated, fly ash/slag paste, Constr. Build. Mater. 81 (2015) 303–312.

[15] S. Puligilla, P. Mondal, Role of slag in microstructural development and hardening of fly ash-slag geopolymer, Cem. Concr. Res. 43 (2013) 70–80.

[16] S. Zhang, A. Keulen, K. Arbi, G. Ye, Waste glass as partial mineral precursor in alkali-activated slag/fly ash system, Cem. Concr. Res. 102 (2017) 29–40.

[17] P.K. Sarker, R. Haque, K.V. Ramgolam, Fracture behaviour of heat cured fly ash based geopolymer concrete, Mater. Des. 44 (2013) 580–586.

[18] Z. Pan, J.G. Sanjayan, B.V. Rangan, Fracture properties of geopolymer paste and concrete, Mag. Concr. Res. 63 (2011) 763–771.

[19] R.J. Thomas, S. Peethamparan, Alkali-activated concrete: engineering properties and stress–strain behavior, Constr. Build. Mater. 93 (2015) 49–56.

[20] C.D. Atiş, C. Bilim, Ö. Çelik, O. Karahan, Influence of activator on the strength and drying shrinkage of alkali-activated slag mortar, Constr. Build. Mater. 23 (2009) 548–555.

[21] P. Nath, P.K. Sarker, Fracture properties of GGBFS-blended fly ash geopolymer concrete cured in ambient temperature, Mater. Struct. 50 (2016) 32.

[22] Y. Ding, C.-J. Shi, N. Li, Fracture properties of slag/fly ash-based geopolymer concrete cured in ambient temperature, Constr. Build. Mater. 190 (2018) 787–795.

[23] M. Ohno, V.C. Li, An integrated design method of Engineered Geopolymer Composite, Cem. Concr. Compos. 88 (2018) 73–85.

[24] B. Nematollahi, J. Qiu, E.-H. Yang, J. Sanjayan, Microscale investigation of fiber-matrix interface properties of strain-hardening geopolymer composite, Ceram. Int. 43 (2017) 15616–15625.

[25] S. Zhang, V.C. Li, G. Ye, Micromechanics-guided development of a slag/fly ash-based strain-hardening geopolymer composite, Cem. Concr. Compos. 109 (2020) 103510.

[26] B. Nematollahi, J. Sanjayan, J. Qiu, E.-H. Yang, Micromechanics-based investigation of a sustainable ambient temperature cured one-part strain hardening geopolymer composite, Constr. Build. Mater. 131 (2017) 552–563.

[27] V.C. Li, H. Stang, Interface property characterization and strengthening mechanisms in fiber reinforced cement based composites, Adv. Cem. Based Mater. 6 (1997) 1–20.

[28] C. Redon, V.C. Li, C. Wu, H. Hoshiro, T. Saito, A. Ogawa, Measuring and modifying interface properties of PVA fibers in ECC matrix, J. Mater. Civ. Eng. 13 (2001) 399–406.

[29] V.C. Li, C. Wu, S. Wang, A. Ogawa, T. Saito, Interface tailoring for strain-hardening polyvinyl alcohol-engineered cementitious composite (PVA-ECC), ACI Mater. J. 99 (2002) 463–472.

[30] E.-H. Yang, Y. Yang, V.C. Li, Use of high volumes of fly ash to improve ECC mechanical properties and material greenness, ACI Mater. J. 104 (2007) 620–628.

[31] Y. Zhou, D. Hou, G. Geng, P. Feng, J. Yu, J. Jiang, Insights into the interfacial strengthening mechanisms of calcium-silicate-hydrate/polymer nanocomposites, Phys. Chem. Chem. Phys. 20 (2018) 8247–8266.

[32] F. Shalchy, N. Rahbar, Nanostructural characteristics and interfacial properties of polymer fibers in cement matrix, ACS Appl. Mater. Interfaces 7 (2015) 17278–17286.

[33] Y. Zhou, D. Hou, H. Manzano, C.A. Orozco, G. Geng, P.J. Monteiro, J. Liu, Interfacial connection mechanisms in calcium–silicate–hydrates/polymer nanocomposites: a molecular dynamics study, ACS Appl. Mater. Interfaces 9 (2017) 41014–41025.

[34] Y. Zhou, L. Tang, J. Liu, C. Miao, Interaction mechanisms between organic and inorganic phases in calcium silicate hydrates/poly(vinyl alcohol) composites, Cem. Concr. Res. 125 (2019) 105891.

[35] J. Du, Y. Bu, Z. Shen, Interfacial properties and nanostructural characteristics of epoxy resin in cement matrix, Constr. Build. Mater. 164 (2018) 103–112.

[36] D. Lau, O. Büyüköztürk, M.J. Buehler, Characterization of the intrinsic strength between epoxy and silica using a multiscale approach, J. Mater. Res. 27 (2012) 1787–1796.

[37] P. Krivenko, Why alkaline activation–60 years of the theory and practice of alkali-activated materials, J. Ceram. Sci. Technol 8 (2017) 323–333.

[38] K. Sankar, A. Sutrisno, W.M. Kriven, Slag-fly ash and slag-metakaolin binders: part II—properties of precursors and NMR study of poorly ordered phases, J. Am. Ceram. Soc. 102 (2019) 3204–3227.

[39] S. Zhang, Z. Li, B. Ghiassi, S. Yin, G. Ye, Fracture Properties and Microstructure Formation of Hardened Alkali-Activated Slag/Fly Ash Pastes, Cem. Concr. Res. 144 (2021) 106447, https://doi.org/10.1016/j.cemconres.2021.106447 (06/01/2021)).

[40] I. García-Lodeiro, A. Fernández-Jiménez, M.T. Blanco, A. Palomo, FTIR study of the sol–gel synthesis of cementitious gels: C–S–H and N–A–S–H, J. Sol-Gel Sci. Technol. 45 (2008) 63–72.

[41] I. Garcia-Lodeiro, A. Palomo, A. Fernández-Jiménez, D.E. Macphee, Compatibility studies between N-A-S-H and C-A-S-H gels. Study in the ternary diagram Na₂O–CaO–Al₂O₃–SiO₂–H₂O, Cem. Concr. Res. 41 (2011) 923–931.

[42] Y. Zuo, Experimental Study and Numerical Simulation of the Reaction Process and Microstructure Formation of Alkali-activated Materials, Delft University of Technology, 2019.

[43] R.J.-M. Pellenq, A. Kushima, R. Shahsavari, K.J. Van Vliet, M.J. Buehler, S. Yip, F.-J. Ulm, A realistic molecular model of cement hydrates, Proc. Natl. Acad. Sci. 106 (2009) 16102–16107.

[44] M.A. Qomi, K. Krakowiak, M. Bauchy, K. Stewart, R. Shahsavari, D. Jagannathan, D.B. Brommer, A. Baronnet, M.J. Buehler, S. Yip, Combinatorial molecular optimization of cement hydrates, Nat. Commun. 5 (2014) 4960.

[45] G. Kovačević, B. Persson, L. Nicoleau, A. Nonat, V. Veryazov, Atomistic modeling of crystal structure of Ca1. 67SiHx, Cem. Concr. Res. 67 (2015) 197–203.

[46] A. Kumar, B.J. Walder, A. Kunhi Mohamed, A. Hofstetter, B. Srinivasan, A. J. Rossini, K. Scrivener, L. Emsley, P. Bowen, The atomic-level structure of cementitious calcium silicate hydrate, J. Phys. Chem. C 121 (2017) 17188–17196.

[47] E. Bonaccorsi, S. Merlino, A.R. Kampf, The crystal structure of tobermorite 14 Å (plombierite), a C–S–H phase, J. Am. Ceram. Soc. 88 (2005) 505–512.

[48] J.M. Martínez, L. Martínez, Packing optimization for automated generation of complex system's initial configurations for molecular dynamics and docking, J. Comput. Chem. 24 (2003) 819–825.

[49] S. Plimpton, Fast parallel algorithms for short-range molecular dynamics, J. Comput. Phys. 117 (1995) 1–19.

[50] K. Chenoweth, A.C. Van Duin, W.A. Goddard, ReaxFF reactive force field for molecular dynamics simulations of hydrocarbon oxidation, J. Phys. Chem. A 112 (2008) 1040–1053.

[51] H. Manzano, S. Moeini, F. Marinelli, A.C. Van Duin, F.-J. Ulm, R.J.-M. Pellenq, Confined water dissociation in microporous defective silicates: mechanism, dipole distribution, and impact on substrate properties, J. Am. Chem. Soc. 134 (2012) 2208–2215.

[52] R. Shahsavari, R.J.-M. Pellenq, F.-J. Ulm, Empirical force fields for complex hydrated calcio-silicate layered materials, Phys. Chem. Chem. Phys. 13 (2011) 1002–1011.

[53] B.R. Brooks, R.E. Bruccoleri, B.D. Olafson, D.J. States, S.a. Swaminathan, M. Karplus, CHARMM: a program for macromolecular energy, minimization, and dynamics calculations, J. Comput. Chem. 4 (1983) 187–217.

[54] M.D. Hanwell, D.E. Curtis, D.C. Lonie, T. Vandermeersch, E. Zurek, G.R. Hutchison, Avogadro: an advanced semantic chemical editor, visualization, and analysis platform, J. Cheminformatics 4 (2012) 17.

[55] C.M. Breneman, K.B. Wiberg, Determining atom-centered monopoles from molecular electrostatic potentials. The need for high sampling density in formamide conformational analysis, J. Comput. Chem. 11 (1990) 361–373.

[56] B. Feuston, S. Garofalini, Empirical three-body potential for vitreous silica, J. Chem. Phys. 89 (1988) 5818–5824.

[57] M. Brehm, B. Kirchner, TRAVIS-A Free Analyzer and Visualizer for Monte Carlo and Molecular Dynamics Trajectories, ACS Publications, 2011.

[58] T. Head-Gordon, G. Hura, Water structure from scattering experiments and simulation, Chem. Rev. 102 (2002) 2651–2670.

[59] J. Rossen, K. Scrivener, Optimization of SEM-EDS to determine the C–A–S–H composition in matured cement paste samples, Mater. Charact. 123 (2017) 294–306.

[60] K. Kjellsen, A. Monsøy, K. Isachsen, R. Detwiler, Preparation of flat-polished specimens for SEM-backscattered electron imaging and X-ray microanalysis—importance of epoxy impregnation, Cem. Concr. Res. 33 (2003) 611–616.

[61] A. Katz, V.C. Li, A special technique for determining the bond strength of micro-fibres in cement matrix by pullout test, J. Mater. Sci. Lett. 15 (1996) 1821–1823.

[62] C. Chen, W. Li, Y. Song, L. Weng, N. Zhang, The effect of geometrical criteria on hydrogen bonds analysis in aqueous glycerol solutions, J. Mol. Imaging Dyn. 1 (2011) 101.

[63] C. Tang, X. Li, Z. Li, J. Hao, Interfacial hydrogen bonds and their influence mechanism on increasing the thermal stability of nano-SiO₂-modified meta-aramid fibres, Polymers 9 (2017) 504.

[64] L. Schaeffer, The role of functional groups in drug–receptor interactions, in: The Practice of Medicinal Chemistry, Elsevier, 2008, pp. 464–480.

[65] K. Scrivener, R. Snellings, B. Lothenbach, A Practical Guide to Microstructural Analysis of Cementitious Materials, Crc Press, 2018.

[66] D. Ravikumar, N. Neithalath, Effects of activator characteristics on the reaction product formation in slag binders activated using alkali silicate powder and NaOH, Cem. Concr. Compos. 34 (2012) 809–818.

[67] S.-D. Wang, K.L. Scrivener, Hydration products of alkali activated slag cement, Cem. Concr. Res. 25 (1995) 561–571.

[68] I. Richardson, A. Brough, G. Groves, C. Dobson, The characterization of hardened alkali-activated blast-furnace slag pastes and the nature of the calcium silicate hydrate (CSH) phase, Cem. Concr. Res. 24 (1994) 813–829.

[69] F. Puertas, S. Martínez-Ramírez, S. Alonso, T. Vazquez, Alkali-activated fly ash/slag cements: strength behaviour and hydration products, Cem. Concr. Res. 30 (2000) 1625–1632.

[70] E. Deir, B.S. Gebregziabiher, S. Peethamparan, Influence of starting material on the early age hydration kinetics, microstructure and composition of binding gel in alkali activated binder systems, Cem. Concr. Compos. 48 (2014) 108–117.

[71] X. Gao, Q.L. Yu, H.J.H. Brouwers, Reaction kinetics, gel character and strength of ambient temperature cured alkali activated slag–fly ash blends, Constr. Build. Mater. 80 (2015) 105–115.

[72] F. Puertas, M. Palacios, H. Manzano, J.S. Dolado, A. Rico, J. Rodríguez, A model for the C-A-S-H gel formed in alkali-activated slag cements, J. Eur. Ceram. Soc. 31 (2011) 2043–2056.

[73] M. Nedeljković, B. Šavija, Y. Zuo, M. Luković, G. Ye, Effect of natural carbonation on the pore structure and elastic modulus of the alkali-activated fly ash and slag pastes, Constr. Build. Mater. 161 (2018) 687–704.

[74] T. Horikoshi, A. Ogawa, T. Saito, H. Hoshiro, G. Fischer, V. Li, Properties of polyvinylalcohol fiber as reinforcing materials for cementitious composites, in: International RILEM Workshop on HPFRCC in Structural Applications, 2006, p. 147.

[75] R.J. Myers, S.A. Bernal, J.L. Provis, A thermodynamic model for C-(N-) ASH gel: CNASH_ss. Derivation and validation, Cem. Concr. Res. 66 (2014) 27–47.

[76] R.J. Myers, B. Lothenbach, S.A. Bernal, J.L. Provis, Thermodynamic modelling of alkali-activated slag cements, Appl. Geochem. 61 (2015) 233–247.

[77] M. Nedeljković, Carbonation Mechanism of Alkali-activated Fly Ash and Slag Materials: In View of Long-term Performance Predictions, Delft University of Technology, 2019.

[78] H. Ye, Nanoscale attraction between calcium-aluminosilicate-hydrate and Mg-Al layered double hydroxides in alkali-activated slag, Mater. Charact. 140 (2018) 95–102.

[79] Y. Zuo, M. Nedeljković, G. Ye, Pore solution composition of alkali-activated slag/fly ash pastes, Cem. Concr. Res. 115 (2019) 230–250.

[80] Z. Lin, V.C. Li, Crack bridging in fiber reinforced cementitious composites with slip-hardening interfaces, J. Mech. Phys. Solids 45 (1997) 763–787.

[81] Z. Lin, T. Kanda, V. Li, On interface property characterization and performance of fiber reinforced cementitious composites, Concr. Sci. Eng. 1 (1999) 173–174.

[82] S. Zhang, Y. Zuo, Z. Li, G. Ye, Isothermal calorimetric study on heat evolution and of apparent activation energy of alkali-activated slag/fly ash pastes, in: 2th International Conference on Sustainable Building MaterialsEindhoven, the Netherlands, 2019.

[83] D. Ravikumar, N. Neithalath, Reaction kinetics in sodium silicate powder and liquid activated slag binders evaluated using isothermal calorimetry, Thermochim. Acta 546 (2012) 32–43.

[84] S. He, Z. Li, E.-H. Yang, Quantitative characterization of anisotropic properties of the interfacial transition zone (ITZ) between microfiber and cement paste, Cem. Concr. Res. 122 (2019) 136–146.

[85] A.R. Sakulich, V.C. Li, Nanoscale characterization of engineered cementitious composites (ECC), Cem. Concr. Res. 41 (2011) 169–175.

[86] Z.P. Bazant, J. Planas, Fracture and Size Effect in Concrete and Other Quasibrittle Materials, CRC Press, 1997.